2022

Microscopic morphomolecular evaluation of transgenic humanized ACE2 murine models of SARS-CoV2

https://hdl.handle.net/2144/45749

Boston University

BOSTON UNIVERSITY

SCHOOL OF MEDICINE

Thesis

MICROSCOPIC MORPHOMOLECULAR EVALUATION OF TRANSGENIC

HUMANIZED ACE2 MURINE MODELS OF SARS-CoV2

by

ANNA TSENG

B.S., California Polytechnic State University, 2020

Submitted in partial fulfillment of the

requirements for the degree of

Master of Science

2022

Approved by

First Reader   _____

Nicholas A. Crossland, D.V.M., DACVP
Assistant Professor of Pathology and Laboratory Medicine
Investigator, NEIDL

Second Reader   _____

Elizabeth Duffy, M.A.
Assistant Professor of Pathology and Laboratory Medicine

MICROSCOPIC MORPHOMOLECULAR EVALUATION OF TRANSGENIC HUMANIZED ACE2 MURINE MODELS OF SARS-CoV-2

ANNA TSENG

ABSTRACT

INTRODUCTION: SARS-CoV-2 is the causative agent for the ongoing pandemic that was first declared in 2020, taking the lives of almost six million people and disrupting communities worldwide. Although an impressive global effort from the scientific community has yielded multiple vaccines and therapeutics, more research is crucial for continued progress against SARS-CoV-2 and future emerging infectious diseases. Animal models have played a significant role in the development of many advancements throughout the pandemic, and better models are needed for more effective research.

OBJECTIVE: Although many animals have been utilized for SARS-CoV-2 research, a model to recapitulate severe pulmonary disease is still lacking. Routinely utilized models have consisted of non-human primates, Syrian hamsters, and mice. Excluding ethical concerns, non-human primates are expensive and limited in supply, limiting the ability to execute more statistically powerful studies. Pneumonia caused by SARS-CoV-2 in non-human primates is also very mild, with nearly all animals surviving, creating substantial skepticism surrounding the frequency of acute respiratory distress syndrome (ARDS) and diffuse alveolar damage (DAD) occurrence in these animal models. Syrian hamsters are also naturally permissive to SARS-CoV-2 and consistently display the most severe lung pathology of any existing animal model, but the lack of availability of species-specific

reagents and research tools makes studying this model difficult. Utilization of mouse model does not require development of new research tools, as mice have been classically utilized for preclinical research for decades. This work seeks to characterize and evaluate two human ACE2-expressing transgenic mouse models to provide the scientific community with knowledge on their translational relevance.

METHODS: K18-hACE2 (K18) and Rosa26-hACE2 (Rosa26) mice were infected with SARS-CoV-2 and checked daily for temperature and weight. Plaque assays and qPCR were utilized to determine viral load. Tissues were stained with H&E for histopathological scoring and qualitative analysis. K18-HACE2and Rosa26-hACE2tissues were fluorescently labeled using two different multiplex immunohistochemistry panels. Slides were digitized by a Vectra Polaris™ fluorescent whole slide scanner, unmixed using inFORM™ vxxx and digital analysis was completed using HALO™ vxxx. Statistical analysis was conducted using GraphPad Prism™ 9.0.1.

RESULTS: Both transgenic models succumbed to SARS-CoV-2 infection, with neurodissemination and death/euthanasia corresponding with peak viral loads in both models. *hACE2* mRNA and ACE2 protein anatomical distribution and expression levels was similar in both models as determined by RNAscope® ISH and IHC respectively. In brains, hACE2 was expressed sporadically in neurons, but consistently in blood vessels and choroidal epithelium. In the lungs, viral load peaked on day 2 and 4 while lung infiltrate steadily increased throughout the course of infection, peaking on day 7- 8. However, severe lung pathology was not observed in any animals and many of the

hallmarks of diffuse alveolar damage were absent, namely the formation of a hyaline membrane, hemorrhage, edema, alveolar fibrin polymerization and neutrophil influx. K18-HACE2 mice showed less lung infiltrate when compared to Rosa26-hACE2mice, which had more T-cell rich infiltrate. No significant difference exists between the two strains in terms of IBA1+ cells and CD11b+ cells in the lungs, though both cell populations increased throughout the course of infection. Both models demonstrated neuroinvasion as early as day 4, but neurodissemination in the Rosa26-hACE2infection was limited to ventral portions of the brain, while the K18-hACE2 showed severe and near global dissemination within the brain aside from cerebellar sparing which was observed in both models. K18-HACE2mice showed a significant decrease in neuronal density and an increase in microglial reactive processes consistent with SARS-CoV-2 induced neuronal loss and microglial reactivity. Together, these findings show that neither hACE2 transgenic mouse model represents a model of severe lung disease for SARS-CoV-2 and that the main determinant of lethality is viral neuroinvasion and neurodissemination. Although hACE2 was under the control of the keratin 18 promoter in both models, the distinct insertion location resulted in distinct clinicopathological outcomes that are not easily explained but bring appreciation to the complexity of the central dogma of biology.

CONCLUSION: Using digital image analysis of immunohistochemistry paired with histopathological scoring and traditional molecular and virological techniques, this study demonstrates that although the transgenic hACE2 mouse models available to researchers result in lethal disease following SARS-CoV-2 infection, death/euthanasia is invariably

resulting of neurodissemination with mild pneumonia limiting their translational

relevance of mirroring severe COVID-19 in humans.

TABLE OF CONTENTS

LIST OF TABLES

LIST OF FIGURES

LIST OF ABBREVIATIONS

AAV……………………………………………………………Adeno-associated virus

ACE2……………………………………………………….Angiotensin-Converting Enzyme 2

ACIP………………………………………….Advisory Committee on Immunization Practices

AF……………………………………………….…………………………Actin Filament

AGM……………………………………………………………….African Green Monkey

AQ……………………………………………………………..Area Quantification

ARDS…………………………………………………….Acute Respiratory Distress Syndrome

AT1…………………………………………………...Alveolar Type I Pneumocyte

AT2………………………………………………………Alveolar Type II Pneumocyte

BSL2……………………………………………………………..Biosafety Level 2

BSL3…………………………………………………………......Biosafety Level 3

BU……………………………………………………………….……Boston University

CCR6……………………………………………………….Chemokine Receptor 6

CDC…………………………………………………………Centers for Disease Control

CNS……………………………………………………………….Central Nervous System

CoV…………………………………………………………………………Coronavirus

COVID-19……………………………………………………Coronavirus Disease 2019

CRISPR………………………..Cluster Regularly Interspaced Short Palindromic Repeats

CT Scan……………………………………………………...Computed Tomography Scan

CTD……………………………………………………….....................C-terminal domain

DAD……………………………………………………………..Diffuse Alveolar Damage

INTRODUCTION

SARS-CoV-2 Background

During the winter of 2019, a turning point in human history occurred with the emergence of an unknown coronavirus from the Hubei province of China. Quickly proliferating and spreading to new hosts, the virus known as severe acute respiratory syndrome coronavirus 2 (SARS-CoV-2) swept through the world, now having left nearly six million people dead (2-27-2022) and many more in critical condition [1]. Hospitals reached maximum capacity, with healthcare workers bearing much of the brunt of the pandemic and testing labs struggling with an overwhelming number of samples to result. As the most severe pandemic to occur during an age of social media and online communication, misinformation spread faster than the virus itself, leading to heightened anxiety, confusion, and astonishment [2]. Unleashed alongside the virus was a wave of xenophobia and racism, particularly against Asians and people of Asian descent, with physical attacks and harassment becoming all-too-frequent headlines [3]. China was heavily scrutinized for a seemingly inadequate response at the start of the pandemic and conspiracies of a cover-up along with more sinister ideas quickly circled around the globe. Many governments responded to the pandemic with mask mandates, social distancing orders, and business shut-downs to avoid congregations of unmasked groups of people, as the virus was shown to be spread through small droplets. In response, many protested these new regulations claiming infringement upon their rights, and several protests against masks took place while the death toll rose. Some of the complaints regarding masks ranged from asthma, acne, "the funk" inside a mask, and even Satanism

[4]. Despite the shock from the general public and questionable responses from governments, two other coronavirus-related health crises have occurred in the last decade and the SARS-CoV2 outbreak could have been better anticipated [5].

Severe Acute Respiratory Syndrome coronavirus (SARS-CoV) emerged in China in 2002, infecting more than two thousand people and killing about four percent of patients, while Middle East Respiratory Syndrome (MERS) was initially discovered in 2012 and infected eighteen hundred with a case fatality of thirty-six percent [6][7]. Two other members of the coronavirus family, HCoV-OC43 and HCoV-229E, are estimated to cause around a third of common colds. The members of this virus family, Coronaviridae, are found in many different mammals and bird species and are thought to have spillover events from bats, mice, and domestic animals. Through phylogenetic studies, it is thought that SARS-CoV is of bat origin that then developed in civets as a secondary host, and MERS-CoV2 was shown to develop in dromedary camels, and a study showed that 90% of dromedary camels had antibodies against MERS-CoV2 [8][9]. SARS-CoV2 has been linked to many potential reservoir populations that ultimately led to the fateful zoonotic event in 2019; white-tailed deer, pangolins, snakes, mink, and perhaps the most widely accepted, horseshoe bats, were all considered possible origins [10][11][12][13][14][15]. Many farms of these animals were shut down and the animals culled for fear of outbreaks spreading to humans, with Denmark ordering the mass slaughter of seventeen million mink only for the corpses to resurface from mass graves and possibly contaminate the water supply [16][17]. Other naturally susceptible hosts include Syrian hamsters, which have been utilized in SARS-CoV2 research. Animal models have been crucial for the

success in developing multiple vaccines available to the public, two of which are the first mRNA vaccines ever approved. Several treatments are also available, including the antiviral remdesivir, and four antibody treatments: sotrovimab, casirivimab/imdevimab, bamlanivimab/etesevimab, and tocilizumab, the latter not targeting SARS-CoV2 itself but instead interleukin-6 (IL-6) to avert dangerous levels of inflammation [18]. Although the successes of the scientific community in response to the pandemic are deserving of apt pomp and circumstance, new variants of SARS-CoV2 are emerging rapidly and threaten the previously-seroconverted masses [19][20]. It is crucial that research continues at this breakneck pace to best prepare for an uncertain future.

Structure and Function of SARS-CoV2

The family name, coronaviridae, comes from the spike protein, which reflects the distinct crowned outer surface of virions when viewed ultrastructurally by electron microscopy. Coronaviruses are considered group IV within the Baltimore classification system, meaning they are enveloped, non-segmented, single-stranded sense RNA viruses, and SARS-CoV2 is one of seven coronaviruses known to infect humans [21]. Coronaviruses have some of the largest genomes of all viruses, and certainly the largest among RNA viruses, and are helical in capsid structure. SARS-CoV1, SARS-CoV2, and MERS are all beta coronaviruses, and are further classified in sublineage A, B, C, or D. Common cold-causing coronaviruses belong to lineage A, SARS-CoV1 and 2 belong to B, and MERS is the first lineage C betacoronavirus known to infect humans [22][23]. Coronaviruses share a similar virion shape, with a highly glycosylated trimer spike (S) protein projecting out

from the membrane component which is used to bind host receptors and induce clathrin-mediated endocytosis [24] [25]. Each of the monomers have an S1 and S2 domain, with the S1 domain from the three monomers entangling to form the ectodomain and the S2 domains comprising the stalk, transmembrane, and small intracellular domains [34]. The receptor binding domain (RBD), a component of S1, binds and opens another cleavage site on S2 [26]. The nucleocapsid protein (N) forms complexes with the gRNA and interacts with other virus proteins to allow for efficient assembly. N has three domains, known as the N terminal domain (NTD), the C-terminal domain (CTD), and the RNA-binding domain; all three domains have been demonstrated to bind viral RNA. It has been proposed that the NTD is able to act in a hand-like manner, with positively charged "fingers" that neutralize RNA phosphate groups and a hydrophobic "palm" to hold the base moieties [27]. In SARS-CoV2 infection, host receptor angiotensin converting enzyme 2 (ACE2) binds with the S protein and the S protein is cleaved by furins, or other transmembrane proteases like serine 2 (TMPRSS2), to expose the S2 subunit containing hydrophobic fusion peptides [28][29][30]. This furin activity seems to play a crucial role in disease susceptibility, as it has been demonstrated that the cleavage of S by furins or furin-like proteins is essential for viral entry into lung cells, and dysregulation of these proteolytic proteins contributes to disease severity in certain populations, like smokers or people with psoriasis [31][32][33] Several other host receptors have been implicated in cell entry, including neuropilin 1 (NRP1) and basigin [34][35]. Fusion of the virus membrane with the endosomal membrane is triggered by a drop in pH or host proteolytic cleavage, and the genome is released into the cytoplasm [30].

The genomic sense RNA, which has thirteen ORFs, is then translated into two polyproteins, pp1a and pp1ab, due to a frameshift that happens between ORF1a and ORF1b. This frameshift favors ppla, leading to 1.4–2.2 times more protein than pplb [36]. Between the two polypeptides, sixteen viral proteins are cleaved via cysteine proteases inside NSP3. ORF1a and ORF1b makeup the first two thirds of the genome, and the last third is transcribed to form a nested set of antisense subgenomic mRNAs that encode structural proteins, similar to class V viruses. These sgRNAs are created as a result of a template switch from a body transcription regulatory sequence (TRS-B) to the leader sequence (TRS-L) at the end of the 5' of the template strand. Since this switch can occur with any of the TRS-Bs, a nested set will result from transcription.

These subgenomic RNAs code for structural and accessory proteins. The roles of many of the 29 SARS-CoV-2 proteins have yet to be determined. Of the eleven accessory proteins, ORF3b, ORF6, ORF7a, and ORF8a have been demonstrated to be potent interferon antagonists [37][38][39][40]. ORF3a is a viroporin that may promote virus release and shares 72.7% of its protein identity with the SARS-CoV ORF3a [41][42][43]. ORF9b may interact with Tom70, a mitochondrial import receptor, to inhibit type I interferon (IFN) synthesis [44]. The nucleocapsid protein (N) serves an important role in virion assembly as it contains an RNA binding domain and a domain that dimerizes the protein when in solution but how N interacts with viral RNA and self assembles into helical filaments or globular viral RNP complexes has yet to be elucidated [45]. Several viral-induced changes can be seen in infected cells, with electron micrographs revealing altered features such as convoluted membranes (CMS), double-membrane bound vesicles

(DMVs), zipper rough endoplasmic reticulum (ZRER), and variable stages of viral particle development including those with peplomers and cross-sections of nucleocapsid aggregates.

Most viruses hijack host cytoskeleton during infection cycle, and coronaviruses are no exception; it has been demonstrated that these viruses can be seen "surfing" the filapodia by altering actin filament (AF) polymerization, using actin for clatharin-mediated uptake, SARS-CoV-2 M protein binding AFs to thicken beneath membrane surface as to potentially provide the force required for budding [46]. As SARS-CoV-2 and other ssRNA viruses utilize a membrane in their virion structure, budding is an essential aspect of viral assembly to acquire host membrane. Nucleocapsid is incorporated into the viral membrane by budding through the intermediate compartment between the ER and the golgi. The M protein is most expressed on the viral membrane, and its presence retains the spike protein within the endoplasmic reticulum [47]. Host cells have anti-budding mechanisms in place, such as tetherin, and SARS-CoV-1 has been demonstrated to inhibit tetherin by blocking its glycosylation with ORF7a. SARS-CoV-2 has been shown to downregulate tetherin, but independent of ORF7a.

Several other mechanisms have been implicated in immune suppression, since understanding SARS-CoV-2 effects on the immune system are crucial for gaining a complete story of the disease as host immune dysregulation is a key characteristic of severe cases. Altering function of the endothelial throws off the immune response, as endothelial cells (ECs) are known to coordinate immunological homeostasis, with

expression of viral, cytokine, and toll-like receptors to further aid the EC response. The endothelial also helps present antigen to CD4 and CD8 cells, though more limited than other professional-presenting cells. The EC also modulates transendothelium migration by upregulating key proteins to allow for myeloid and lymphoid cells to roll until they reach the site of infection, where they can be activated and undergo endothelial transmigration into tissues. ECs also help memory CD8 cells mature into cytotoxic cells and the differentiation of TH17 cells in response to IL-6. In severe SARS-CoV-2 infection, a "cytokine storm" characterizes later stage infection, and ECs play a critical role in signal amplification with cytokine production and attracting immune-cells to further inflammation [48].

Monocytes are also highly recruited to inflammation during SARS-CoV-2 infection, and many differentiate into dendritic cells (DCs) or macrophages. Large numbers of CD16+ monocytes infiltrate tissue, and classical CD16-CD14+ monocytes only return to normal numbers in recovering patients. Classical monocytes have been shown to have increased expression of IL1β and a pattern of IFN-activation, which undoubtedly contributes to the "cytokine storm". Data from COVID patients regarding monocyte-secreted cytokines is scarce and conflicting, but type 1 IFN response was consistent in most studies. Monocytes are crucial to recovery from SARS-CoV-2 and have been shown to be protective in some animal models, but some evidence also shows that monocytes can be permissive to SARS-CoV-2 infection themselves as they express ACE2. Studies show that SARS-CoV-2 can efficiently infect monocytes but the infection yields an unproductive replication cycle. It has been proposed that SARS-CoV-2 uses this as an

advantage, inducing immunoparalysis since infection was associated with immunoregulatory cytokine secretion and the induction of a macrophagic specific transcriptional program characterized by the upregulation of M2-type molecules. Decreased numbers of monocytes are observed concurrently with the upregulation of immunoregulatory molecule CD163 in patients [49]. Post-mortem analysis of patients who died of COVID-19 revealed infected CD169+ macrophages in lymph nodes and spleen. Infection and exposure to live and heat-inactivated virus resulted in a cytokine profile of IL-6, IL-10, TNF, IL-1, TGF-B, but a lack of IFN supporting the finding that SARS-CoV-2 is able to inhibit interferon response.

Lymphopenia and especially drops in CD4 and CD8 T-cells are a characteristic of SARS-CoV-2 infection, with severe cases showing an even more substantial drop than mild cases. B and NK depletion has also been observed but the drop is less significant (~1.5 fold). The mechanism for SARS-CoV-2 induced lymphopenia remains unknown, but it may be due to hyperactive T-cells leading to a pro-apoptotic state. However, the role of T cells in severe disease remains relatively unknown. Some studies showed a correlation of a lack of robust T-cell response in deceased patients, and others showed stronger T-cell response correlated with severe disease. B-cell response also varied, with patients demonstrating a high heterogeneity of antibodies, with up to a third showing very low titers and a range of neutralizing antibody activity. What research has revealed is that the immune response to SARS-CoV-2 is diverse and different between patients and more studies are undoubtedly necessary to clear up the conflicting data documenting immune response.

Pathogenesis in humans

SARS-CoV, MERS, and SARS-CoV2 can manifest as acute pneumonia and potentially cause death, but many cases consist of flu-like symptoms that resolve in a couple days. SARS-CoV-2 hospitalization may involve the use of ventilators and oxygen tanks due to the destruction of lung tissue, and many people have reported still being affected months after discharge, with reports of at least one organ function impairment three months post infection [50]. It is spread between people by small droplets or direct contact, although the latter is less common. Disease presents symptoms on average 6.4 days post exposure, with the most common symptom being fever followed by cough [51]. Cases are classified by mild, moderate, and severe and the induced pneumonia is categorized into two stages: early and late phase. In the early phase, the virus targets the respiratory system and causes damage directly by virus-mediated tissue damage. In the late phase, the host immune system is activated and secretes a variety of cytokines to organize and mount an effective response. However, in severe COVID-19, hyperinflammatory cytokines, including interleukin (IL)-6, tumor necrosis factor-alpha (TNF-a), and IL-1b can reach extremely high levels and cause systemic inflammation dubbed a "cytokine storm". Diffuse alveolar damage (DAD) is a pathological finding observed in severe disease, characterized by bilateral neutrophil recruitment and infiltrate, edema, and the formation of a hyaline membrane [52]. Gas exchange is disrupted and patients become hypoxic. Severe cases progress approximately 8-9 days following symptom onset and can continue to acute respiratory distress syndrome (ARDS) where more aggressive treatment with ventilators and oxygen may be necessary.

Disease varies greatly among individuals, but consistent trends of several comorbidities and health equity considerations play a vital role in predicting outcome. A classic computed tomography (CT) scan for a SARS-CoV-2 patient shows bilateral ground-glass opacity in sub-pleural regions of the lungs and widespread inflammation. Air sacs fill with fluid, limiting oxygen absorption and leading to classic symptoms of a respiratory virus. Blood workup reveals leukocytosis and can show several abnormalities, including hypolobation, toxic granules in neutrophils, atypical granules in lymphocytes, granulation of chromatin in monocytes, giant platelets and thrombocytopenia and normocytic normochromic anemia [53].

Several other organs have been implicated in SARS-CoV-2 infection, including the heart, gastrointestinal tract (GI), liver, kidney, and central nervous system (CNS). Myocardial injury is a common finding of SARS-CoV-2 cardiovascular manifestation and one study found that 8% of all patients involved had myocardial injury defined as high-sensitivity cardiac troponin (hs-cTn) above the 99th percentile of its upper limit of normal or evidence of myocardial injury in an electrocardiogram. Severe cases had a 13-fold higher risk of myocardial injury, and it was found that hs-cTn was an excellent predictor for disease severity and mortality even after adjusting for comorbidities. ACE2 expression has been demonstrated on myocardial cells, suggesting direct infection is feasible but yet to be proven, on top of the numerous cytokines that can cause vascular inflammation, myocarditis, and cardiac arrhythmias. Acute coronary syndrome has also been linked to SARS-CoV-2, and has many possible factors influencing its prevalence, including hypercoagulability, proinflammatory cytokines, stress, and altered endothelium.

Gastrointestinal dysfunction is another common finding of SARS-CoV-2 with symptoms including diarrhea, anorexia, and nausea occurring in 2-10% of cases [54]. The mechanism by which SARS-CoV-2 causes GI symptoms remains unknown, but ACE2 has also been shown to be expressed throughout intestinal mucosa, and pro-inflammatory cytokines have been shown to cause gastric distress. Hepatic injury is observed in many SARS-CoV-2 patients in the form of deranged liver enzymes. Declining liver function is associated with worse prognosis and a prolonged hospital stay and seems to be caused by direct viral cytopathic effects, medication, and anoxia [55]. Congruent findings for the cause of renal injury point to similar mechanisms, with the resulting manifestation as increased serum creatinine, variable degrees of proteinuria and hematuria, and radiographic abnormalities of the kidneys [56]. Infection of neurons have also been a concern throughout the pandemic, with many research groups claiming the virus is capable of neuroinvasion. Case reports of mood changes shortly before hospitalization and viral RNA in the brain are toted as evidence of neuroinvasion, but conclusive evidence of viral proteins in the brain is very limited. Studies have demonstrated that the virus is capable of infecting neurons from experiments showing a colocalization of viral proteins inside neurons and the classic COVD-19 symptom of losing smell and taste [57]. It is clear that multifactorial injury of organs outside of the respiratory system should provide a new perspective on respiratory illness.

Common medical conditions that place a person at higher risk of severe illness from SARS-CoV-2 infection include cancer, chronic kidney disease, chronic liver disease, chronic lung disease, dementia or other neurological conditions, type 1 or 2 diabetes,

down syndrome, heart conditions, HIV and other immunocompromising conditions, mental health conditions, overweight and obesity, pregnancy, sickle cell or thalassemia, smoking, organ or stem cell transplantation, substance use disorders, tuberculosis, and high blood pressure. Other studies have begun to shed light on health equity playing a significant role on SARS-CoV-2 outcome, with several factors such as race, education, occupation, income, and housing investigated as being associated with more cases, hospitalizations, and deaths. Unintended consequences of mitigation strategies also can disproportionately affect mental health, bereavement, food insecurity, unemployment, housing instability, and healthcare services in general for people in minority groups. Several studies documenting homelessness demonstrate that people experiencing homelessness make up a disproportionate 2% of the total SARS-CoV-2 hospitalizations, despite making up less than .2% of the US population [58].

Therapeutic options and vaccine development

Research and pharmaceutical companies were able to generate several vaccine options for the general public in a matter of a few months following the outbreak. Healthcare workers were able to receive their first dose of vaccine within a year of the pandemic onset, with the general public following shortly after. This impressive feat was partly due to an established body of knowledge about coronaviruses from SARS, MERS, and other common cold coronaviruses. Many different platforms of vaccine technology are utilized to create an effective vaccine against SARS-CoV-2, often with the goal of preventing severe illness. Most vaccines that have proceeded to and past clinical trials focus on the spike protein to elicit an effective antibody generation. Currently, there are three FDA

approved vaccines in the US approved for SARS-CoV-2 in the general public: Pfizer, Moderna, and the Janssen vaccines. The former two are the first FDA-approved mRNA vaccines, relying on lipid nanoparticles (LNP) to protect and carry the mRNA to muscle cells and produce spike protein, which is presented on major histocompatibility complex I (MHC I). The immune system reacts and generates antibodies against the spike protein [59]. These vaccines were designed to be given in two doses, and an additional booster is now available for the public. The Pfizer and Moderna vaccines are approved for use in most other countries, either by emergency use or have been fully authorized at this point. The Janssen vaccine is an adenovirus-vector vaccine, which utilizes a viral vector expressing the spike protein of SARS-CoV-2 to generate an immune response. With all current adenovirus-vector vaccines, the adenovirus is altered by replacing the E1 gene to eliminate replication competency by inserting the full-length SARS-CoV-2 spike gene. The E3 gene is also removed [60]. The Janssen clinical trial was praised for being one of the most inclusive, prioritizing diversity and different backgrounds for its study, and eliminating participants who already had antibodies to SARS-CoV-2. It requires only one dose, but numerous cases of thrombosis with thrombocytopenia syndrome and Guillain-Barre syndrome have been reported and the Centers for Disease Control and Prevention (CDC) recommends mRNA vaccines over the Janssen vaccine. Johnson and Johnson, the parent company, has since suspended production of the vaccine. Other viral vector vaccines either in clinical trials or approved for use include the Oxford-AstraZeneca vaccine (Oxford University and AstraZeneca collaboration), Sputnik V (Gamaleya Research Institute of Epidemiology and Microbiology in Russia), Sputnik Light

(Gamaleya Research Institute of Epidemiology and Microbiology in Russia), and Convidecia [61]. Other platforms for vaccine development include: DNA plasmid-based vaccine ZyCoV-D (Cadila Healthcare) which is approved in India, inactivated virus vaccines such as Sinopharm BIBP (Sinopharm), CoronaVac (Sinovac), Covaxin (Bharat Biotech), Sinopharm WIBP (Sinopharm), and CoviVac (Chumakov Centre), and subunit vaccines like Novavax (Novavax), Abdala (Center for Genetic Engineering and Biotechnology in Cuba), EpiVacCorona (VECTOR center of Virology), ZifiVax (Anhui Zhifei Longcom in collaboration with the Institute of Microbiology at the Chinese Academy of Sciences), and Soberana 02 (Finlay Institute). Some concerns regarding inactivated virus vaccines include the inactivation step altering S protein confirmation and even causing the S1 component to detach. Many of these vaccines rely on the adjuvant aluminum hydroxide to further stimulate the immune system.

SARS-CoV-2 therapeutics have also advanced substantially throughout the pandemic, with monoclonal antibodies and small molecule antivirals aiding many SARS-CoV-2 patients. There are many targets for COVID-19 therapeutics, including viral structural proteins, nonstructural proteins, accessory proteins, and host genes, epigenetics, and other host pathways [62]. Remdesivir was the first COVID-19 treatment approved by the FDA for hospitalized patients at least 12 years of age. It works as an adenosine nucleoside triphosphate analog, which interferes with the viral RNA-dependent RNA polymerase, usually leading to a premature and irreversible chain termination [63]. It was originally developed as a drug for hepatitis C and studied in the context of filoviruses before being utilized in COVID-19 infections [64]. Other antivirals are approved for emergency action

use (EAU), including Pfizer's Pazlovid and Merck's molnupiravir. Monoclonal antibodies are also used, including Actemra, Bebtelovimab, Evusheld, Casirivimab, Imdevimab, Etesevimab, and Sotrovimab [65][66]. Convalescent plasma is also used in COVID-19 patients, as it is blood plasma from people who had recovered and produced antibodies against the virus. Many other treatments are still under development as the scientific community continues tirelessly.

Non-human primate and human models

With their similarity to humans, non-human primates (NHPs) are ideal models for biomedical research. There are many research tools available to NHP research, as most human tools cross react with NHP targets. However, their high demand and ethical concerns regarding their role make a stable supply difficult. With SARS-CoV-2 research, obtaining NHPs became increasingly challenging and the cost of these animals continues to carry a hefty price. The husbandry of NHPs is also complicated, and together, these factors make reaching sufficient numbers for powerful studies exceedingly expensive [67]. SARS-CoV-2 infection in NHPs has also proven to be mild in almost all cases, with almost none developing ARDS. Both rhesus and cynomolgus macaques rarely show clinical signs, and minimal pathological changes with minimal amounts of lung consolidation observed in most animals [68]. Multifocal to coalescing areas of pneumonia was observed in lung parenchyma, with some alveolar necrosis and alveolar type II (AT2) pneumocyte hyperplasia. Edema was found in many alveolar spaces, along with some fibrin, neutrophils, alveolar macrophages, and lymphocytes. In bronchioles, denudated epithelium along with plump AT2 pneumocytes representing regeneration are

noted in some animals. By day 15, animals show only small areas of consolidation and an increase of bronchial-associated lymphoid tissue (BALT) in some animals. Similar findings were observed in other NHPs, including African green monkeys (AGM) [69]. Since the disease is transient and mild in macaques and AGMs, this recapitulates most human disease but does not offer researchers insight into severe disease. For this reason, many vaccine and therapeutic studies relied on antibody generation instead of development of clinical symptoms. A model of severe disease is still desperately needed to evaluate therapeutics intended for hospitalized COVID-19 patients.

Human challenge studies have been highly debated throughout the pandemic, as historically, these studies have had major impact in vaccine and therapeutic development. A dark connotation goes along with these types of experiments, as German and Japanese experiments during World War II, the Tuskegee Study, Willowbrook hepatitis experiments, and more taint the benefits a more ethically designed experiment could reap. Debate around how to design such a study has continued throughout the debate, with concerns that such studies will contain a sample bias of willing participants and that compensation could take advantage of certain populations. United Kingdom COVID-19 challenge trials are currently underway, interested in immune responses that protect people from re-infection [70]. Participants are compensated financially, medical care provided, and the study claims to have adequate mechanisms for informed consent. The high payment may be attractive to those less privileged, but the study was widely advertised and not intended to target any marginalized groups. In any case, the study will serve as a precedent for future human roles in infectious disease studies, perhaps paving

the way for future ethical academic human experiments.

Small animal models

Since NHPs present their challenges to researchers particularly in the economic burden,

small animal models are essential for modern research. Their simple housing and

husbandry, as well as rapid breeding, allow researchers ease designing studies with

sufficient power. The Institutional Animal Care and Use Committee (IUCUC) outlines

how laboratory animals are to be treated, and rodents are simpler to use in research for

this reason as well. Several small animals have been utilized in SARS-CoV-2 research,

but the most common are mice and Syrian hamsters. The latter is naturally susceptible to

SARS-CoV-2, but is relatively new to the world of infectious disease research, with few

research tools developed. Syrian hamsters are now commonly used in many SARS-CoV-

2 studies, ranging from elucidating the role of viral proteins to effects of COVID-19 on

testicle size[71]. Most hamsters show mild-to-moderate disease with some weight loss,

and after about two weeks, the animals nearly invariably recover. Pneumonia is most

severe around 5-7 dpi with peak viral load around day 2 [72]. Subsequent immune

infiltrate with monomorphonuclear cells and neutrophils and congestion of blood vessels

accompany these pathological changes. Pneumonia can be seen as patchy lesions that

affect both lungs, with some marked perivascular cuffing. Hyaline membranes, a key

finding of DAD, are not seen in hamsters and animals rarely succumb to disease.

Differences in sex and age seen in humans are also replicated in Syrian hamsters [73].

For these reasons, Syrian hamsters are considered the best current animal model to

recapitulate moderate to severe self-limiting lung disease.

However, due to a lack of research tools for hamsters, a mouse model for severe disease is still highly sought. Unlike Syrian hamsters, mice are not naturally permissive to the virus, with the exception of some VOC (beta and gamma), and further alterations to the model must initially take place to confer permissibility. The viral S protein does not have a high affinity for mouse ACE2, so several different approaches to this dilemma have been developed; these include a mouse adapted SARS-CoV-2 strain, an adenovirus-associated-virus (AAV)-transduced or knock-in mouse, a fetal lung xenograft (fLX) model, and the focus of this study, the transgenic (tg) mouse expressing human ACE2 (hACE2) [73]. The mouse-adapted virus model can be created from passing SARS-CoV-2 through mouse lung tissue. Mutations in the viral RNA genome will make any mutant virions that can infect mouse ACE2 advantageous as they will have higher levels of replication. Another approach is to modify the binding domain of the virus to be able to bind mouse ACE2. This model has varying reports of disease, with many research groups reporting a failure to reproduce pathology seen in humans. The translational potential for this model is very limited; a further complication of this platform is that since the virus is not the same virus that infects humans, vaccines and therapeutics may have different efficacies. Instead of altering the virus to infect mice, other models modify the host itself to express hACE2. The AAV-transduced mouse model relies on a vector to transduce lung epithelium to express hACE2, using a CRISPR/Cas9 technology. This is advantageous in that it is flexible in mouse strain, but the expression of hACE2 between animals can be highly variable and fails to reproduce severe lung pathology [74]. The

fLX model is also meant to use the human-infecting strain of SARS-CoV-2, but in human tissue as well. Using a mouse deficient in the lymphocytic compartment of the immune system, small pieces of competent human fetal lungs are engrafted on the mouse's back in the subcutaneous space. The mouse can be given human immune cells too, to study human immune responses in the context of human tissue. However, this model is very costly to produce and highly variable between animals. Donor tissues originate from many different sources as well as composition, meaning a range of immune responses and cell types develops within the tissue, and the success rate of the engraftment adds additional variation in the model. This model also fails to show multisystemic impacts of disease. The transgenic mouse model is engineered to be able to express hACE2 in all epithelial tissues by using an epithelial promoter, cytokeratin 18 (K18) for the ACE2 gene insertion. These mice are created by inserting hACE2 with the K18 promoter into a location within the mouse's genes, and these mice can be bred and continue to pass on the inserted gene. They have been used in numerous studies of SARS-CoV-2, which some claim the mice die from severe respiratory disease, and others claiming neuroinvasion. Viral replication occurs in the AT2 and AT1 pneumocytes, and never in bronchioles, again with the exception of some VOCs (beta). Neutrophils and macrophages follow shortly after viral replication is seen in the interstitium, and lymphocytic infiltrate can be seen on day 4 and after. Very little edema, denudated epithelium, hemorrhage, and other signs of DAD are observed in the lungs of tg mice. Many studies fail to conduct lung inflations, which are necessary to determine much of the lung pathology, which perhaps explains why literature reports vary widely. Reports of

neuroinvasion are persistent throughout literature. [75][76][77] A summary of different

mouse models can be viewed in **Table 1**.

Model	Creation	Benefit	Limitations
Mouse adapted SARS-CoV-2 strain	Attenuated SARS-CoV-2 in mouse tissue	Able to infect wild-type mice	Largely fails to reproduce pathology Mouse-adapted virus has different efficacies with treatments and vaccines intended for human use with the human strain of SARS-CoV-2
AAV-transduced or knock-in mouse	Using a viral vector to add hACE2 to target cells at the DNA level	short time to construct flexible in mouse strain	Fails to show severe pathology High variability of hACE2 expression based on success of transduction
Human Fetal Lung Xenograft mouse	Engrafting fetal human lung tissue on the backs of immunocompromised mice	captures dynamics in human tissue with human strain of virus	High variability of donor composition leading to high variability of graft High cost
Transgenic mouse expressing hACE2	Insertion of hACE2 into germ line	Uses human strain of virus Simple to breed	Neuroinvasion Failure to replicate severe lung pathology

Table 1. Comparison of various animal models of SARS-Cov-2 infection.

Research models

In this study, two tg mouse models will be compared: the K18-hACE2 and Rosa26-hACE2 models. The K18-hACE2 mouse was developed by McCray et al in 2007 to study SARS-CoV-1, which also uses hACE2 but the mouse was disregarded after evidence of neuroinvasion potentially confounded data. With the K18 promoter, hACE2 is expressed mainly in airway epithelial cells and enterocytes lining the colonic mucosa, with lesser amounts found in kidney, liver, spleen, and small intestine, and scant levels of expression in the brain. The insertion of the gene is random, and several different strains of K18-HACE2mice have been created, with varying amounts of hACE2 expression depending on the insertion location and number of hACE2 copies within the insertion. The mice used within this study are from the Jackson Laboratory and have eight insertions in a single site on chromosome 2.

The Rosa26-hACE2, developed by Taconic, also uses the K18 promoter and the same hACE2 gene, but the insertion is not random; it is targeted toward the Rosa26 locus, a well-characterized section of chromosome 6 that has been useful for gene insertion. ROSA stands for Reverse Orientation Splice Acceptor, a relic of its first application, and is spliced into three exons that are not translated to a protein. By inserting a gene into the integration site, no potential downstream effects come from the targeted insertion, unlike with a random insertion. This mouse model is not well characterized, and no previous literature exists describing this model. It has a single copy of the hACE2 gene, unlike the K18-hACE2's 8 copies. **Figure 1** describes the insertion of the K18-hACE2 cassette via recombinase-mediated cassette exchange (RMCE) into the Rosa26 locus.
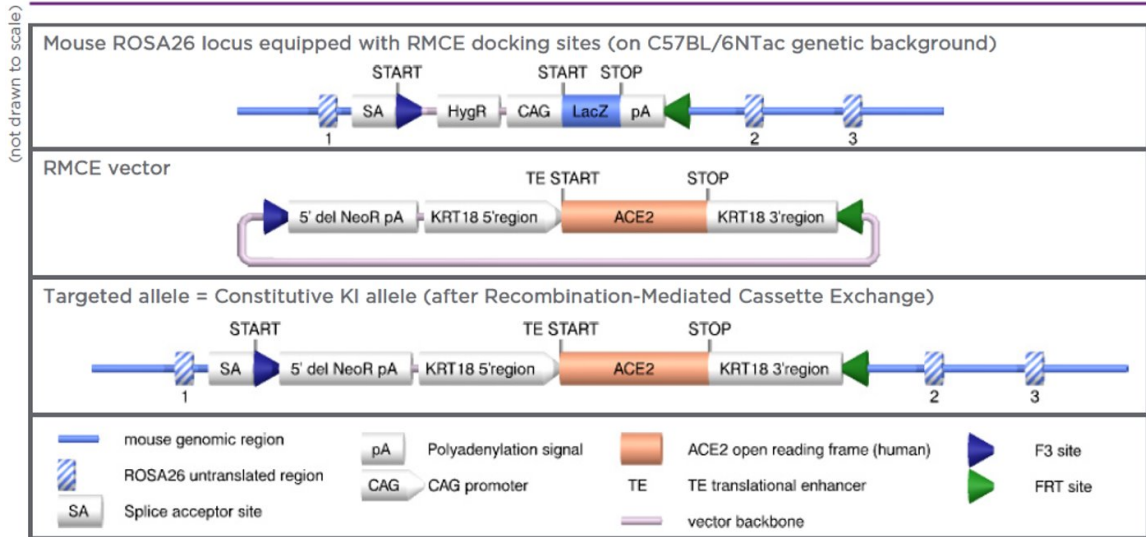
Figure 1: Insertion of the K18-hACE2 cassette into the Rosa26 locus using recombinase-mediated cassette exchange (RMCE). Docking sites within the ROSA26 locus allow the RMCE to find the correct location within the genome and site-specific recombinases swap the RMCE vector with the existing cassette. The result is a cassette swap in cells permissive to the AAV carrying the RMCE vector.

METHODS

Biosafety

All aspects of this study were approved by the Institutional Biosafety Committee and theoffice of Environmental health and Safety at Boston University prior to study initiation. All work with SARS-CoV-2 was performed in a biosafety level-3 (BSL3) laboratory by qualified personnel equipped with powered air-purifying respirators. Following euthanasia and necropsy, tissues were chemically inactivated for a minimum of 72 hoursbefore being taken out of the BSL3 space. Upon certification of inactivation, the remaining work was done in a biosafety level-2 (BSL2) laboratory.

Mice

Mice were maintained in a facility accredited by the Association for the Assessment and Accreditation of Laboratory Animal Care (AAALAC). All protocols were approved by the Boston University Institutional Animal Care and Use Committee (PROTO202000020). Heterozygous K18-hACE2 C57BL/6J mice of both sexes (strain: 2B6.Cg-Tg(K18-ACE2)2Prlmn/J) were obtained from the Jackson Laboratory (Jax, Bar Harbor, ME). Rosa26-hACE2 mice were obtained from Taconic Biosciences (Rensselaer, NY). Animals were group-housed by sex in Tecniplast green line individually ventilated cages (Tecniplast, Buguggiate, Italy). Mice were maintained on a 12:12 light cycle at 30-70% humidity and provided ad-libitum water and standard chow diets (LabDiet, St. Louis, MO).

Intranasal inoculation with SARS-CoV-2.

At 12–16 weeks of age, K18-hACE2 and Rosa26-hACE2 mice of both sexes were intranasally inoculated with a low (1 x 10^4 PFU), intermediate (1 x 10^5 PFU), or high dose (1 x 10^6 PFU) of SARS-CoV-2 in 50 µl of sterile 1X PBS (K19-hACE2 [10^4 N = 15 10^5 N = 22 10^6 N = 35] Rosa26-hACE2 [10^4 N = 7 10^5 N = 19 10^6 N = 7]], or sham inoculated with 50 µl of sterile 1X PBS. Inoculations were performed under 1-3% isoflurane anesthesia and the survival curve was evaluated up to 14 dpi. Test mice were inoculated with the intermediate dose (1 x 10^5 PFU) and euthanized at 2 dpi, 4 dpi, 7 dpi or terminal disease after having reached euthanasia criteria. For H&E and monoplex IHC analysis, thirty-three animals were examined, which included Sham/PBS inoculated negative controls (n=4). For the multiplex lung panel, twenty-five animal lungs (12 Rosa-26 hACE2 and 13 K18-hACE2) were examined including 3 Sham/PBS inoculated negative controls (1 K18-hACE2, 2 Rosa26-hACE2).

mice have better survival at the low dose than K18-hACE2 mice (10^4 N = 15 10^5 N = 22 10^6 N = 35).

Clinical monitoring. Animals included in the 14-day survival curve studies (n=50 infected and n=6 sham) were intraperitoneally implanted with an RFID temperature-monitoring microchip (Unified Information Devices, Lake Villa, IL, USA) 48–72 hours prior to inoculation. An IACUC-approved clinical scoring system was utilized to monitor disease progression and establish humane endpoints (Table 1). Categories evaluated included body weight, general appearance, responsiveness, respiration, and neurological signs for a

maximum score of 5. Animals were considered moribund and humanely euthanized in the event of the following: a score of 4 or greater for 2 consecutive observation periods, weight loss greater than or equal to 20%, severe respiratory distress, or lack of responsiveness. Clinical signs and body temperature were recorded once per day for the duration of the study. For design of the survival curve, animals euthanized on a given day were counted dead the day after. Animals found dead in cage were counted dead on the same day.

Tissue processing and viral RNA isolation.

Tissues were collected from mice and stored in 600 µl of RNA*later* (Sigma-Aldrich; # R0901500ML) and stored at -80 °C. For processing, 20 – 30 mg of tissue were placed into a 2 ml tube with 600 µl of RLT buffer with 1% β-mercaptoethanol and a 5 mm stainless steel bead (Qiagen, Valencia, CA; #69989). Tissues were homogenized using a Qiagen TissueLyser II (Qiagen; Germantown, MD) by two dissociations cycles (two-minutes at 1,800 oscillations/minute) with a one-minute rest in between. Samples were centrifuged at 17,000 X g (13,000 rpm) for 10 minutes and supernatant was transferred to a new 1.5 ml tube. Viral RNA isolation was performed using a Qiagen RNeasy Plus Mini Kit (Qiagen; #74134), according to the manufacturer's instructions. RNA was finally eluted in 30 µl of RNase/DNase-free water and stored at -80 °C until used.

Quantification of infectious particles by plaque assay.

Quantification of SARS-CoV-2 infectious particles were quantified by plaque assay. After euthanizing mice, tissues were collected in 600 µL of RNA*later* (ThermoFisher Scientific, AM7021) and stored at -80 °C until analysis. The day prior to experiments, 24-well plates

containing 8x10^4 Vero E6 cells per well were plated. Between 20-40 mg of tissue was weighed out and placed into a 2 ml tube containing 500 µl of OptiMEM (ThermoFisher) and a 5mm Steal Bead (Qiagen #69997). For the brain, to reduce bias by selecting only non-permissive or highly permissive regions, tissue sampling was performed on several regions throughout the brain including the olfactory bulb, cerebral cortex (left and right side), and cerebellum. Tissues were then homogenized using a Qiagen TissueLyser II (Qiagen; Germantown, MD) by two dissociations cycles (two-minutes at 1,800 oscillations/minute) with a one-minute rest in between. Samples were then subject to centrifugation with a benchtop centrifuge at 17,000 X g (13,000 rpm) for 10 minutes and supernatant was transferred to a new 1.5 ml tube. From this, 1:10 – 1:10^6 dilutions were made in OptiMEM and 300 µl of each dilution were plated onto 12-well plates and incubated at 37 °C for 1 hour with gentle rocking of the plate every 10 minutes. After viral adsorption, 1 ml of a 1:1 mixture of 2X DMEM containing 4% FBS 1% penicillin/streptomycin and 2.4% Avicel (Dupont) was overlaid into each well. Cells were then incubated for 3 days at 37°C with 5% CO_2. After incubation, Avicel was removed, cells were washed with 1X PBS, and fixed in 10% formalin for 1 hour. After fixation, formalin was removed, cells were stained with 0.1% crystal violet in 10% ethanol/water for 1 hour and washed with tap water. Plates were then dried, the number of plaques were counted, and infectious particles (PFU/mg of tissue) were calculated.

RNA isolation from serum.

Total viral RNA was isolated from serum using a Zymo Research Corporation Quick-RNA™ Viral Kit (Zymo Research, Tustin, CA; #R1040) according to the manufacturer's

instructions. RNA was eluted in 15 µl of RNase/DNase-free water and stored at -80 °C until used.

SARS-CoV-2 E-specific reverse transcription quantitative polymerase chain reaction (RT-qPCR).

Viral RNA was quantitated using single-step RT-quantitative real-time PCR (Quanta qScript One-Step RT-qPCR Kit, QuantaBio, Beverly, MA; VWR; #76047-082) with primers and TaqMan® probes targeting the SARS-CoV-2 E gene as previously described[45]. Briefly, a 20 µl reaction mixture containing 10 µl of Quanta qScript™ XLT One-Step RT-qPCR ToughMix, 0.5 µM Primer E_Sarbeco_F1 (ACAGGTACGTTAATAGTTAATAGCGT), 0.5 µM Primer E_Sarbeco_R2 (ATATTGCAGCAGTACGCACACA), 0.25 µM Probe E_Sarbeco_P1 (FAM-ACACTAGCCATCCTTACTGCGCTTCG-BHQ1), and 2 µl of template RNA was prepared. RT-qPCR was performed using an Applied Biosystems QuantStudio 3 (ThermoFisher Scientific) and the following cycling conditions: reverse transcription for 10 minutes at 55 °C, an activation step at 94 °C for 3 min followed by 45 cycles of denaturation at 94 °C for 15 seconds and combined annealing/extension at 58 °C for 30 seconds. Ct values were determined using QuantStudio™ Design and Analysis software V1.5.1 (ThermoFisher Scientific). For absolute quantitation of viral RNA, a 389 bp fragment from the SARS-CoV-2 E gene was cloned onto pIDTBlue plasmid under an SP6 promoter using NEB PCR cloning kit (New England Biosciences, Ipswich, MA). The cloned fragment was then *in vitro* transcribed (mMessage mMachine SP6 transcription kit; ThermoFisher) to generate an RT-qPCR standard.

H&E histopathological evaluation

5µm sections were prepared from FFPE (formalin-fixed, paraffin-embedded) lung

tissueand transferred to glass slides. Tissue samples were deparaffinized and stained

with hematoxylin and eosin (H&E) using a combined Leica Autostainer-coverslipper

unit ST5010-CV5030 (Leica Microsystems, Wetzlar, Germany). Images were

analyzed by Dr. Nicholas Crossland, a board-certified veterinary pathologist, in order

to determine key pathological features within the tissues. Lungs were given an ordinal

score of 1-5 based on severity. Lung and brains were scored based on spike IHC on a

scale of 1 to 3, with a summary of the histologic and IHC score findings in Table 5.

Brightfield Immunohistochemistry

Antigen retrieval was conducted using a Tris based buffer-Cell Conditioning 1 (CC1)-

Catalog # 950-124 (Roche). The SARS-CoV-2 spike and ACE2 primary antibodies were

of rabbit origin, and thus developed with a secondary goat anti-rabbit HRP-polymer

antibody (Vector Laboratories, Burlingame, CA) for 20min at 37C. Brightfield slides

utilized A ChromoMap DAB (3,3′-Diaminobenzidine) Kit-Catalog #760-159 (Roche) to

form a brown precipitate at the site of primary-secondary antibody complexes

containing HRP. Slides were counterstained with hematoxylin and mounted.

Fluorescent multiplex immunohistochemistry (mIHC) with tyramide signal

amplification (TSA)

Fluorescence mIHC with TSA was conducted using Akoya Bioscience's Opal Dye Kit.

Automated mIHC was run on a Ventana Discovery Ultra (Roche, Basel, Switzerland).

Before multiplex-IHC was performed, each antibody was individually optimized using a single-plex-IHC assay using an appropriate positive control tissue. Optimizations were performed to determine ideal primary antibody dilution, sequential order of antibody development, assignment of each primary antibody to an Opal fluorophore, and fluorophore dilution. Once an optimal protocol was established, 5µm tissue sections were cut from FFPE mouse tissue. All Opal TSA-conjugated fluorophore reactions took place for 20 minutes. Fluorescent slides were counterstained with spectral DAPI (Akoya Biosciences) for 16 minutes before being mounted with ProLong gold antifade (ThermoFischer). An overview of the TSA mIHC workflow is provided in **Figure 2.** Antibodies utilized in 5plex 6 color (DAPI counterstained) analysis included: (Panel 1) SARS-CoV-2 Spike protein, IBA1 a monocyte/macrophage marker, CD8 a cytotoxic T-cell marker, CD3e a general T-cell marker, and CD11b a monocyte and neutrophil marker or (Panel 2) SARS-CoV-2 Spike protein, IBA1 a monocyte/macrophage marker, GFAP an astrocyte marker, NeuN a mature neuron marker, and CD31 an endothelial marker. Optimized conditions for these assays are provided in **Table 3** and **Table 4**.
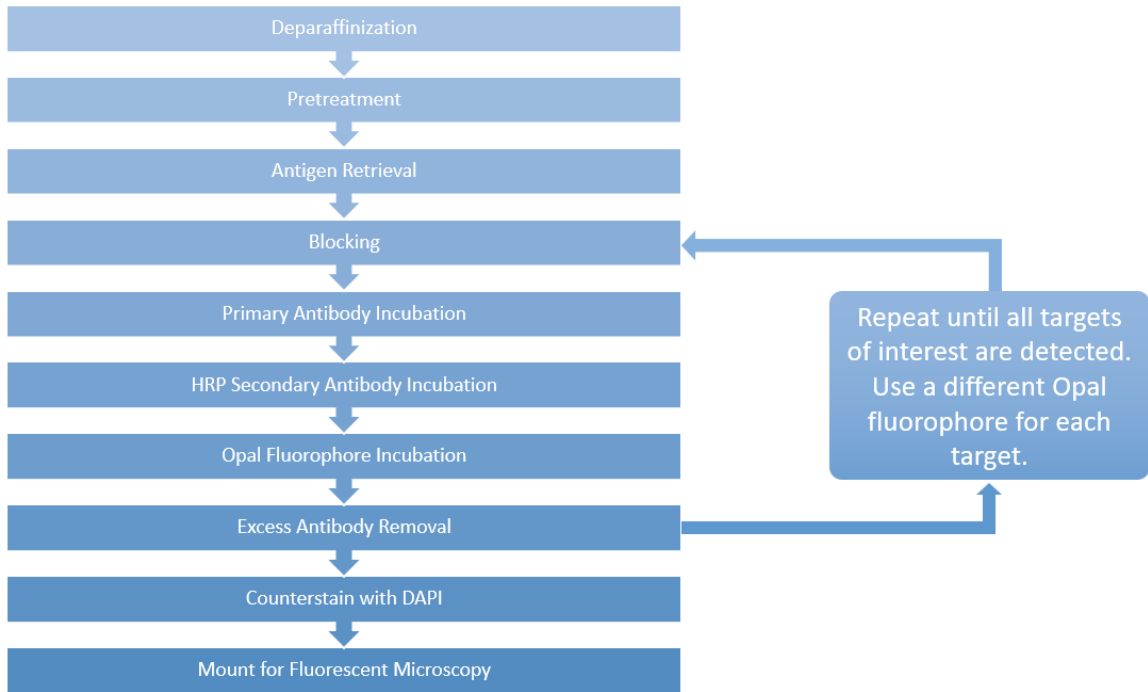
Figure 2. Workflow of fluorescent multiplex IHC with TS

Table 2. Optimized conditions for mIHC panel 1							
Sequential Order	Antibody	Manufacturer, Catalog #	Antibody Dilution	Antibody Incubation	Opal Dye	Manufacturer, Catalog #	Opal Dye Dilution
1	SARS-CoV-2 Spike Protein	Cell Signaling Technologies 99423S	1:400	37, 32 minutes	Opal 570	AkoyaBioSciences, 1488001KT	1:250
2	CD11b	Abcam Ab133357	1:2000	37°C, 32 minutes	Opal 520	AkoyaBioSciences, FP1497001KT FP1487001KT	1:120
3	CD8	Cell Signaling Technologies 98941	1:200	37°C, 32 minutes	Opal 620	AkoyaBioSciences, FP1495001KT	1:60
4	CD3e	Biocare Medical CP215A	1:100	37°C, 60 minutes	Opal 480	AkoyaBioSciences, FP1500001KT	1:100
5	Iba1	WAKO 019-19741	1:2000	37°C, 40 minutes	Opal 690	AkoyaBioSciences, FP1497001KT	1:125

Table 2. Optimized conditions for mHIC panel 1.

Table 3. Optimized conditions for mIHC panel 2							
Sequential Order	Antibody	Manufacturer, Catalog #	Antibody Dilution	Antibody Incubation	Opal Dye	Manufacturer, Catalog #	Opal Dye Dilution
1	SARS-CoV-2 Spike Protein	Cell Signaling Technologies 99423S	1:400	37, 32 minutes	Opal 570	AkoyaBioSciences, 1488001KT	1:250
2	NeuN	Cell Signaling Technologies 24307	1:200	37°C, 40 minutes	Opal 480	AkoyaBioSciences, FP1500001K T	1:150
3	GFAP	Dako, Z0334	1:500	37°C, 64 minutes	Opal 520	AkoyaBioSciences, FP1487001K T	1:320
4	CD31	Cell Signaling Technologies 77699S	1:100	37°C, 64 minutes	Opal 620	AkoyaBioSciences, FP1495001K T	1:80
5	Iba1	WAKO 019-19741	1:2000	37°C, 40 minutes	Opal 690	AkoyaBioSciences, FP1497001K T	1:90

Table 3. Optimized conditions for mIHC panel

RNAscope® In-situ Hybridization (ISH)

For SARS-CoV-2 RNAscope® ISH, an anti-sense probe targeting *hACE2* (GenBank accession number NM_021804.3; Cat. No. 848038) with no cross-reactivity to murine *Ace2* was employed. Using an RNAscope 2.5 LSx Reagent Kit (Advanced Cell Diagnostics, Newark, CA) on the automated BOND RXm platform (Leica Biosystems, Buffalo Grove, IL), four-micron sections of FFPE tissue was subjected to automated baking and deparaffinization followed by heat-induced epitope retrieval (HIER) using a ready-to-use EDTA-based solution (pH 9.0; Leica Biosystems) at 100 °C for 15 min. Subsequently, tissue sections were treated with a ready-to-use protease (RNAscope® 2.5 LSx Protease) for 15 min at 40 °C followed by a ready-to-use hydrogen peroxide solution for 10 min at room temperature. Slides were then incubated with the ready-to-use probe mixture for 2 h at 40 °C, and the signal amplified using a specific set of amplifiers (AMP1 through AMP6 as recommended by the manufacturer). The signal was detected using a Fast-Red solution for 10 minutes at room temperature. Slides were counterstained with a ready-to-use hematoxylin for 5 min, followed by five washes with 1X BOND Wash Solution (Leica Biosystems) for bluing. Slides were finally rinsed in deionized water, dried in a 60 °C oven for 30 min, and mounted with Ecomount® (Biocare, Concord, CA, USA). Murine *peptidylprolyl isomerase B (Ppib)* mRNA was used as a housekeeping gene to determine RNA quality and a Vero E6 cell pellet was used as a positive assay control. For all assays, an uninfected mouse was used as a negative control.

Whole slide scanning and digital image analysis of mIHC

Fluorescently labeled slides were imaged using a Vectra Polaris TM Quantitative

Pathology Imaging System (Akoya Biosciences). Exposures for all Opal dyes on the

Vectra were set based upon regions of interest with strong signal intensities to minimize

exposure times and maximize the specificity of signal detected. Whole slide images were

segmented into smaller QPTIFFs, uploaded into Inform software version 2.4.9 (Akoya

Biosciences), unmixed using spectral libraries affiliated with each respective opal

fluorophore including removal of autofluorescence, then fused together as a single whole

slide image in HALO (Indica Labs, Inc., Corrales, NM). A whole slide scan with

annotated regions is shown in **Figure 3.**

Figure 3. Whole slide scan of mouse brain with annotations taken from an uninfected
Rosa26-hACE2mouse. The yellow line designates a layer for whole midbrain analysis,
while the red is specific for the hippocampus, green for thalamus and hypothalamus, and
teal for cerebral cortex.

Image analysis of monoplex immunohistochemistry

For quantifying the area of the slide that contained SARS-CoV2 Spike, an algorithm called the HALO (Indica Labs) Area Quantification (AQ) module (v2.1.11) was created and finetuned to quantify the immunoreactivity for the Spike protein based on color and stain intensity. Minimum dye intensity thresholds were established using the real-time tuning field of view module to accurately detect positive immunoreactivity. This algorithm outputted the percent of total area displaying immunoreactivity across the annotated whole slide scan in micrometers squared (μm^2). A visual example of an AQ output using HALO™ is shown in Figure 4. Lung consolidation was classified using the tissue random forest tissue classifier module in HALO (Indica Labs), which was developed by annotating each tissue type via manual annotations. These annotations were extensively examined for any errors by the machine-learning classifier and manually excised as necessary. An example of the tissue classifier is shown in Figure 5.

Image analysis of multiplex immunohistochemistry

Digitized whole slide scans were analyzed using the image analysis software HALO (Indica Labs, Inc., Corrales, NM). Visualization threshold values were adjusted in viewer settings to reduce background signal and fine-tune visibility of markers within each sample. Brains were annotated within the midbrain region, with separate layers for thalamus and hypothalamus, cortex, and hippocampus. Lung slides were manually annotated to select regions of interest, excluding heart and adipose tissue. Quantitative outputs of IBA1 from panel 1 and IBA1 and NeuN from panel 2 were obtained using the

AQ module. For quantifying the absolute number and overall percentage of cells expressing various proteins in either mIHC panel, we utilized the Halo (Indica Labs) HighPlex (HP) phenotyping modules (v4.0.4). In brief, this algorithm was used to first segment all cells within the annotated lung sections using DAPI counterstain. Detection threshold and nucleus geometry were defined until segmentation appeared accurate. Next, minimum nucleus, cytoplasm and membrane thresholds were set for each fluorophore to detect low and high expression within each of the segmented cells. Parameters were set using the real-time tuning mechanism that was tailored for each individual sample based on signal intensity. Outputs are shown in **Figure 6.**

Statistical analysis of brightfield histopathology, monoplex IHC, and mIHC

Descriptive statistics and graphics as well as Kaplan-Meier (survival) curves and statistical tests were performed using GraphPad Prism v9.3.1 statistical analysis software (GraphPad, San Diego, CA). Clinical parameters and quantitative pathology results were analyzed using either a two-way or one-way ANOVA. Tests were performed to determine the presence of statistical significance between unmatched groups: control, 2DPI, and 7DPI. Sidak's and Tukey's multiple comparison tests were utilized to determine differences in between groups. GraphPad Prism 9.0.1 was used for all statistical analyses and formulation of graphical depictions of results.
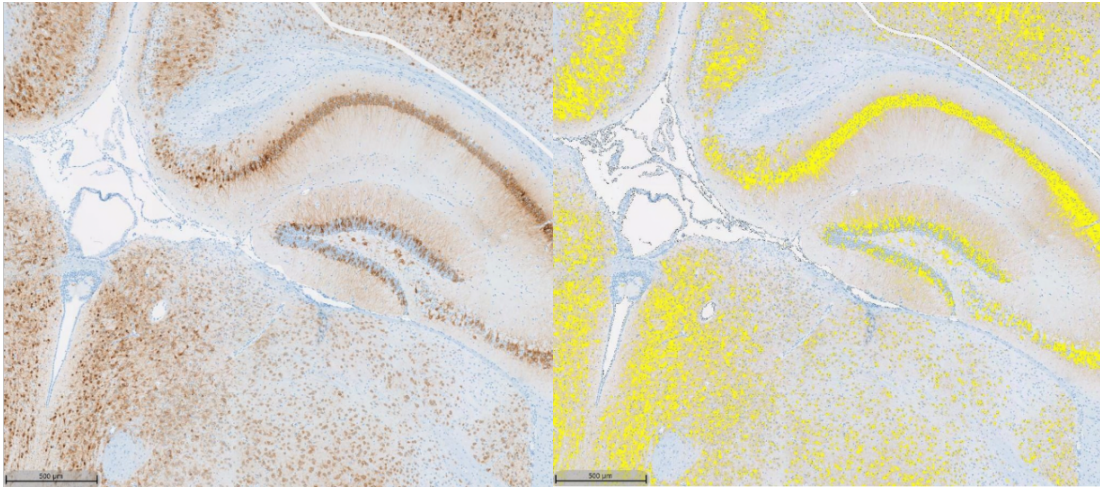
Figure 4. Visual output of area quantification module in HALO™. (A) Raw brain image with DAPI in blue and Spike immunoreactivity in brown. (B) Correlating output of Spike AQshown in yellow.
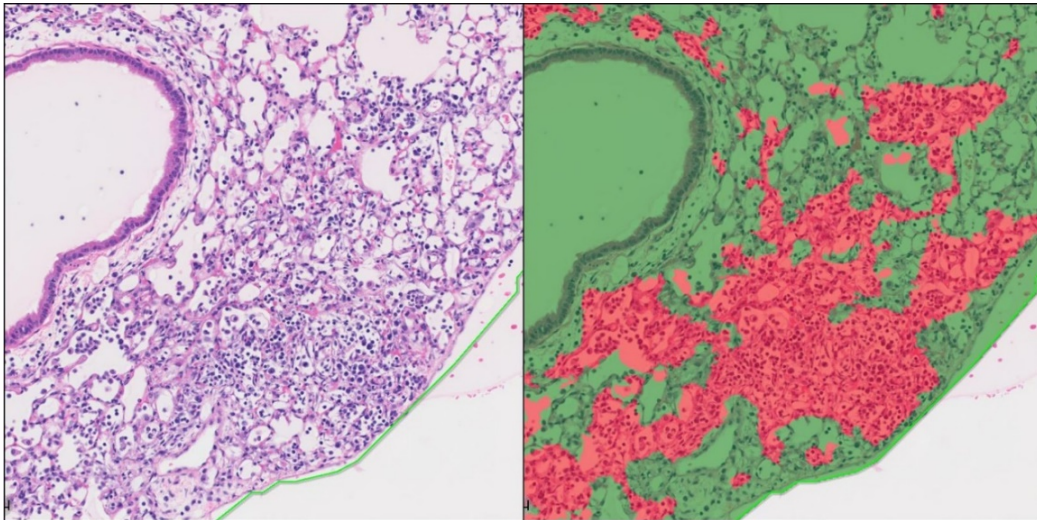
Figure 5. Visual output of Tissue Classifier in HALO™. Red – classified as pneumonia Green – classified as normal. (A) Raw image. (B) Tissue Classifier visual output.
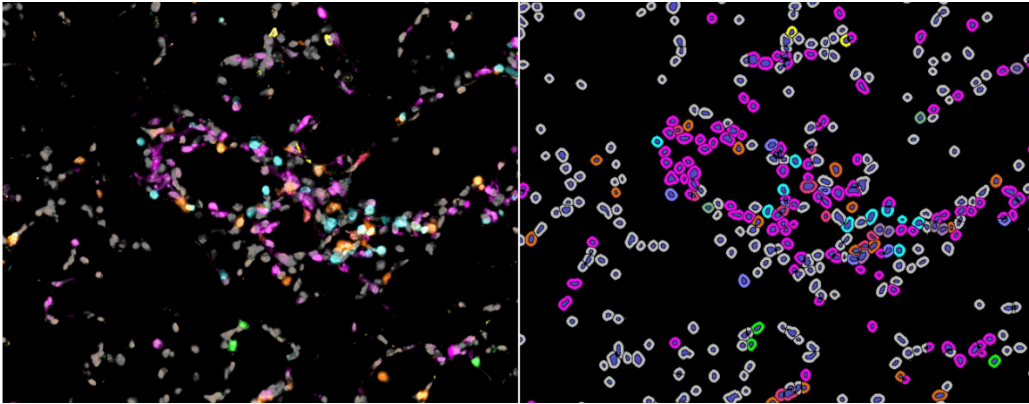
Figure 6. Visual output of multiplex phenotyping in HALO™. DAPI – grey, CD3e – teal, CD11b – green, SARS-CoV-2 Spike – Yellow, CD8 – Orange, IBA1 - magenta. (A) Raw Image. (B) Cell phenotyping visual output.

RESULTS

K18-hACE2 and Rosa26-hACE2 show no discernible differences in hACE2 mRNA or protein expression

By comparing hACE2 IHC in K18-hACE2 and Rosa26-hACE2, little differences in immunoreactivity can be observed between the two strains. Positive staining on the apical membrane of bronchiole epithelium is evident and an occasional AT2, not AT1 cells. There is cross reactivity with the mouse ACE2, so RNAscope® ISH was employed to better observe the expression of *hACE2* mRNA. As illustrated in Figure 7, puncta can be observed where the probe hybridized with hACE2 mRNA in bronchiole epithelium and sporadic AT2 cells. No AT1 cells showed puncta consistent with IHC results. Within the brain, *hACE2* mRNA expression was low in comparison to lung, and its distribution involved clusters of neurons within the cerebral cortex, hippocampus, midbrain, brainstem, and Purkinje cells from the cerebellum. No clear difference between the two mouse strains is obvious with RNAscope® ISH (Figure 7A-L).
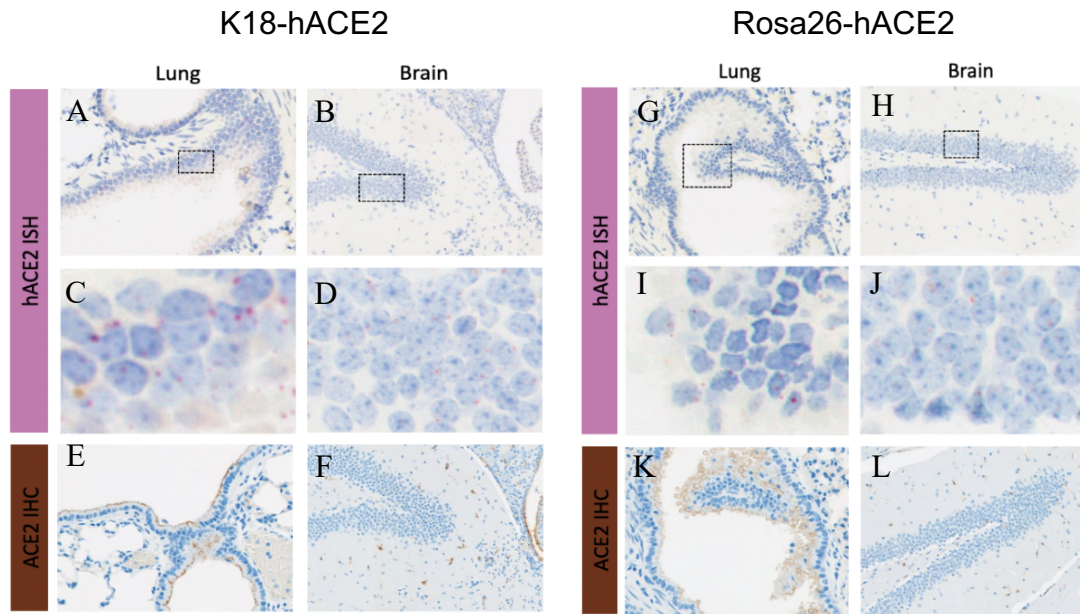
Figure 7: ACE2 IHC and RNAscope® ISH to determine ACE2 expression in tg mouse models. (A) K18-hACE2 lung ACE2 ISH showing anatomical location of C. (B) K18-hACE2 brain ACE2 ISH showing anatomical location of D (C) High magnification of A to show ISH puncta, demonstrating hACE2 mRNA expression within bronchioles. (D) High magnification of B to show ISH puncta, showing limited hACE2 mRNA expression within hippocampal neurons. (E) K18-hACE2 lung ACE2 IHC showing ACE2 expression on apical surface of bronchiole epithelium. (F) K18-hACE2 brain ACE2 IHC showing sporadic ACE2 expression endothelium. (G) Rosa26-hACE2 lung ACE2 IHC showing ISH showing anatomical location of I. (H) Rosa26-hACE2 lung ACE2 IHC showing ISH showing anatomical location of J. (I) High magnification of G to show ISH puncta, demonstrating hACE2 mRNA expression within bronchioles and in comparable expression to K18-hACE2. (J) High magnification of H to show ISH puncta, demonstrating very limited hACE2 mRNA expression within hippocampal neurons and in comparable expression to K18-hACE2. (K) Rosa26-hACE2 lung ACE2 IHC showing ACE2 expression on apical surface of bronchiole epithelium, similar to the K18-hACE expression. (L) Rosa26-hACE2 brain ACE2 IHC showing ACE2 expression in blood vessels.

K18-hACE2 mice are more susceptible to SARS-CoV-2 than Rosa26-hACE2 mice

K18-hACE2 and Rosa26-hACE2 mice inoculated intranasally with SARS-CoV-2 (K18-hACE2 n=33 Rosa26-hACE2 n=8) began losing weight as early as 4 days post-infection (dpi) irrespective of sex, with maximum weight loss occurring at 6-7 dpi. Subsequent drops in body temperature followed, highly associated with declining clinical health. Both SARS-CoV-2-infected K18-hACE2 and Rosa26-hACE2 mice exhibited neurological signs starting 6 dpi, but the K18-hACE2 presented more severe stupor, tremors, proprioceptive defects, and abnormal gait. Many male mice presented severe urinary bladder distention observed at necropsy. Most K18-hACE2 and Rosa26-hACE2 animals were euthanized or found dead in their cage by 8 dpi and survival at an intermediate dose is similar for both strains (Figure 8). This corresponds with increasing viral presence in the brain, with peaking spike immunoreactivity in terminal animals. Brain spike percentage, as calculated by the AQ module, is highly associated with temperature drops (Fig. 9). Contrary to mortality, lung spike peaks on day 2 and 4, and declines in terminal animals (Fig. 10). Molecular methods, PFU and qPCR data, corroborates lung spike AQ percentage and shows that the Rosa26-hACE2 mice show less viral replication than the K18-hACE2 model (Figure 11).
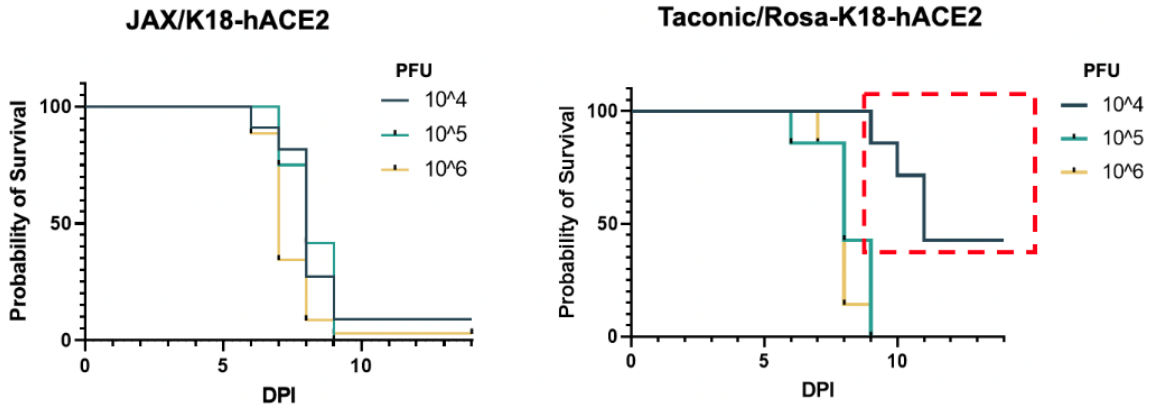
Figure 8: Survival curves of K18-hACE2 and Rosa26-hACE2 mice at various doses of SARS-CoV-2 Rosa26-hACE2 (10^4 N = 7 10^5 N = 19 10^6 N = 7) mice have better survival at the low dose than K18-hACE2 mice (10^4 N = 15 10^5 N = 22 10^6 N = 35).
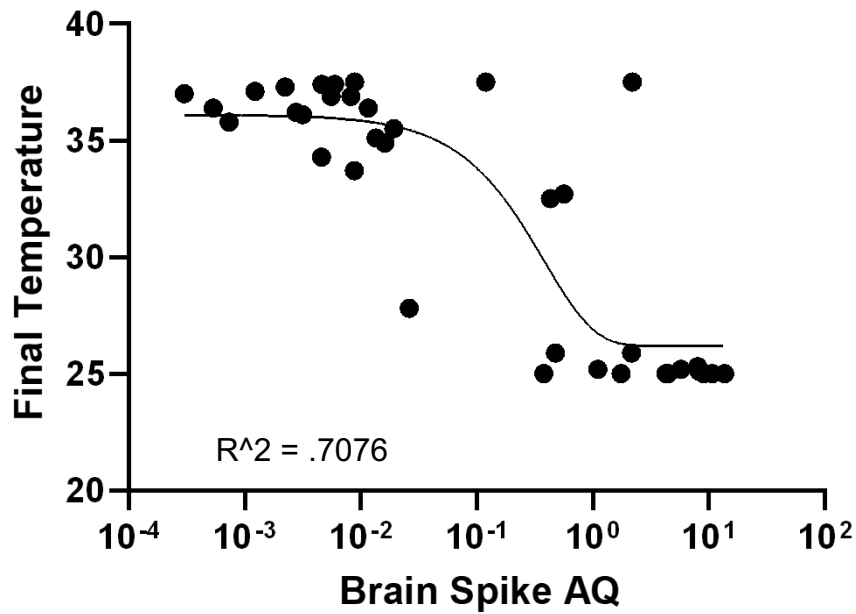
Figure 9: Viral neuroinvasion is highly associated with lowered body temperature. (N=34) Nonlinear regression with one phase decay fit on logarithmic base ten axis.
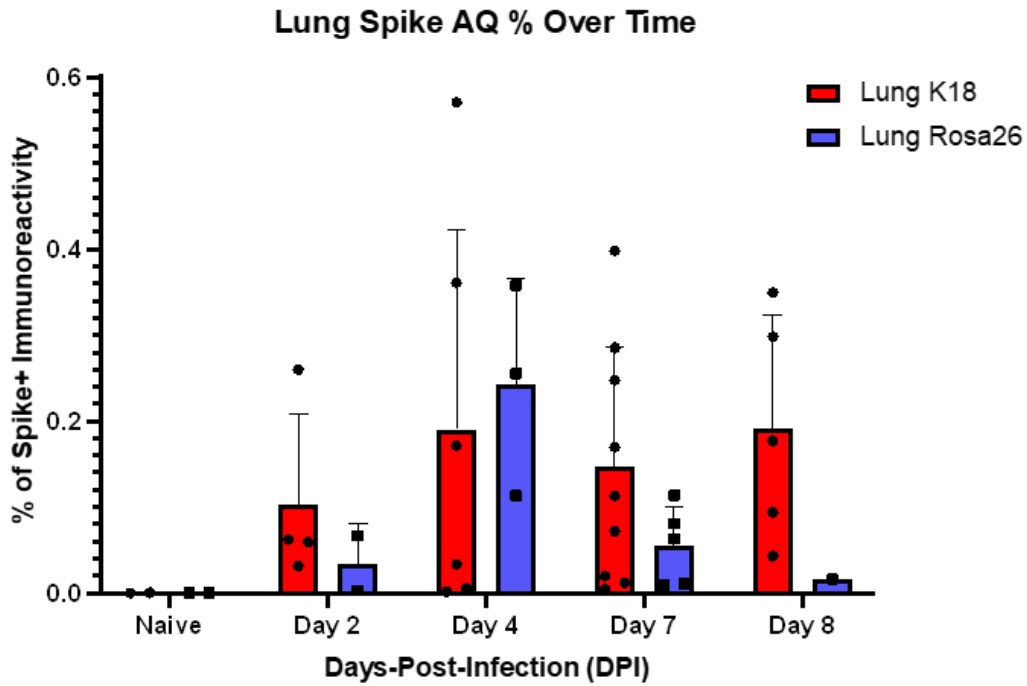
Figure 10: Lung spike AQ% shows Rosa26-hACE2 are less susceptible to viral replication than K18-hACE2 mice, but a high degree of variability exists between animals.
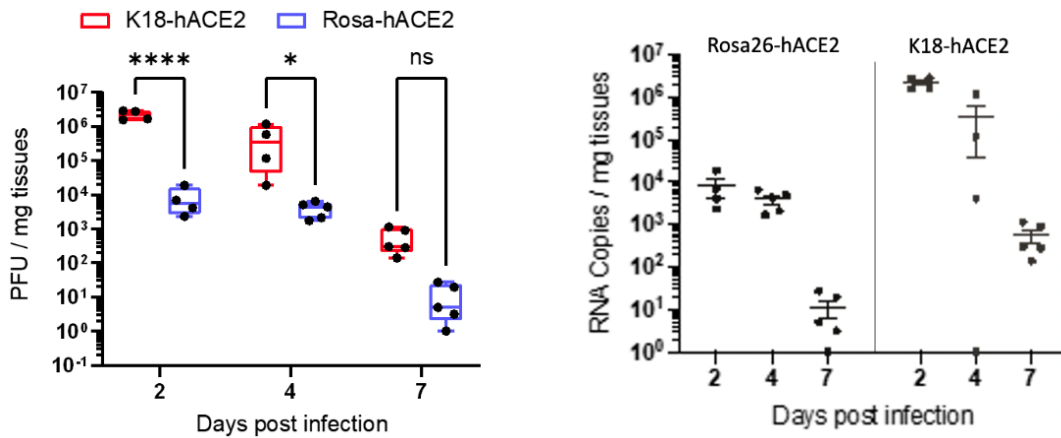
Figure 11: PFU and qPCR data corroborates lung spike AQ%, showing that Rosa26-hACE2 are less susceptible to viral replication than K18-hACE2 mice

Rosa26-hACE2 mice show more lung infiltrate and consolidation

In the lung, pulmonary parenchyma pathology was mainly limited to small regions of attenuation. Lung consolidation steadily increased, peaking in terminal animals **with a statistically significant difference between the strains. (Terminal P = 0.0009)** (Fig. 12A, B, C, D). The lymphocytic infiltrate could be seen in the interstitium and alveoli, but not affecting bronchioles. When looking at the total percentage of lung showing pneumonia using a machine learning classifier, peak consolidation was confirmed to occur at 7 dpi (stats Fig. 13). Rosa26-hACE2 mice shows statistically significant (p<0.05) lung consolidation compared to K18-hACE2 in terminal animals, albeit total lung mean involvement was < xxxx% in both strains indicating the mild severity of pneumonia.
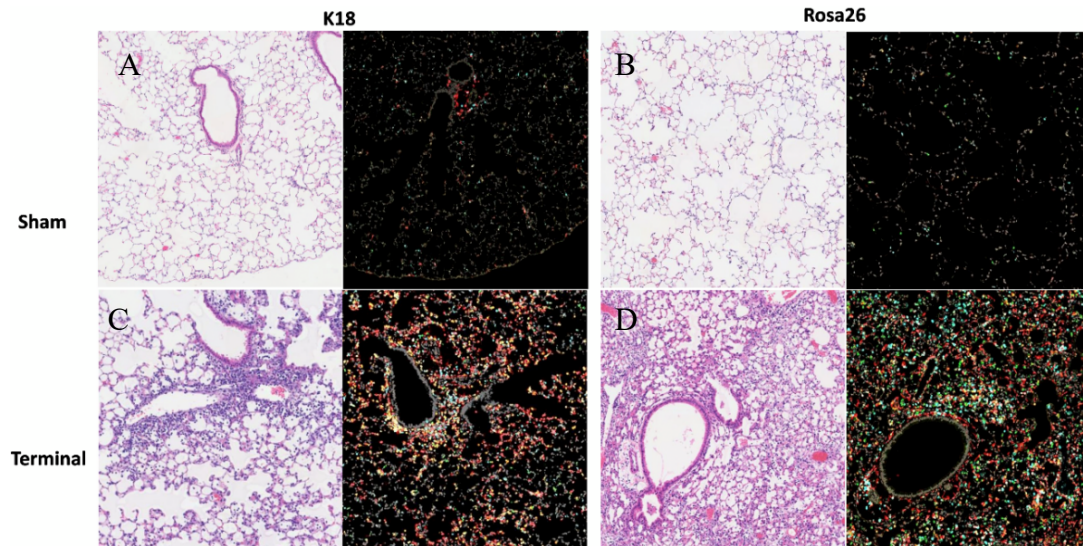
Figure 12: Representative serial sections stained with H&E and mIHC panel 1 comparing sham animals to terminal animals. DAPI – grey, CD3e – teal, CD11b – green, SARS-CoV-2 Spike – Yellow, CD8 – Orange, IBA1 - red (A) K18-hACE2 sham mouse showing normal lung histology, with few immune cells present. (B) Rosa26-hACE2 sham mouse show normal lung histology, similar to the K18-hACE2 sham mouse. (C) K18-hACE2 terminal mouse showing lung infiltrate comprised of both lymphocytic and myeloid lineage cells. (D) Rosa26-hACE2 terminal mouse showing more severe lung infiltrate than the K18-hACE2 terminal mouse, with more lymphocytes present and more lung consolidation.
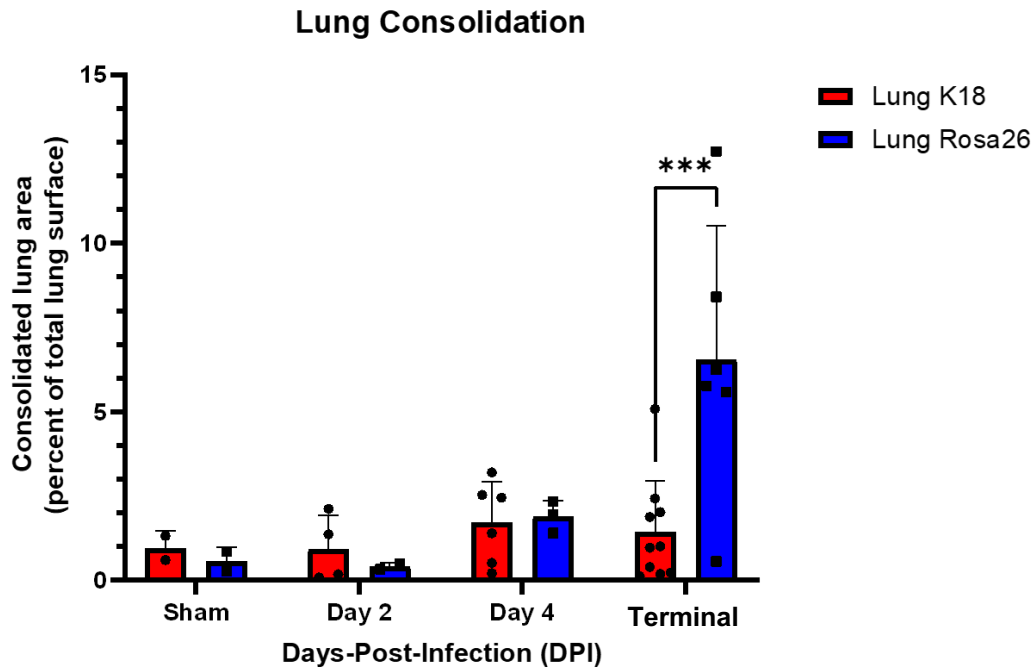
Figure 13: Lung consolidation percentage by HALO classifier module showing more lung infiltrate and consolidation in Rosa26-hACE2 mice. Terminal mice show statistically significant difference between strains (P = 0.0009)

Lung infiltrate is mostly IBA1+ cells for both strains, with Rosa26-hACE2 infiltrate being more T-cell rich

IBA+ immunoreactivity percentage continued to increase over time, peaking in terminal animals (Fig. 14). Rosa26-hACE2 mice show slightly higher average IBA1+ immunoreactivity compared to K18-hACE2 mice, and a larger sample size may show significance in this finding. However, no statistical difference between the strains within the included animals was demonstrated. To better characterize cell types potentially responsible for the differing infiltrate amounts between the strains, a HP algorithm was employed. By phenotyping cells with the HP algorithm designed for mIHC panel 1, CD3e+ revealed Rosa26-hACE2 infiltrate to be more T-cell dense than K18-hACE2 and a significant difference can be observed in terminal animals (P = 0.0322) (Fig. 15). CD11b+ cells do not increase dramatically, unlike other cell populations and the cells that are CD11b+ are not IBA1+, showing these cells are not migrating monocytes. No difference in CD11b+ infiltrate is shown between the two tg mouse strains (Fig. 16).
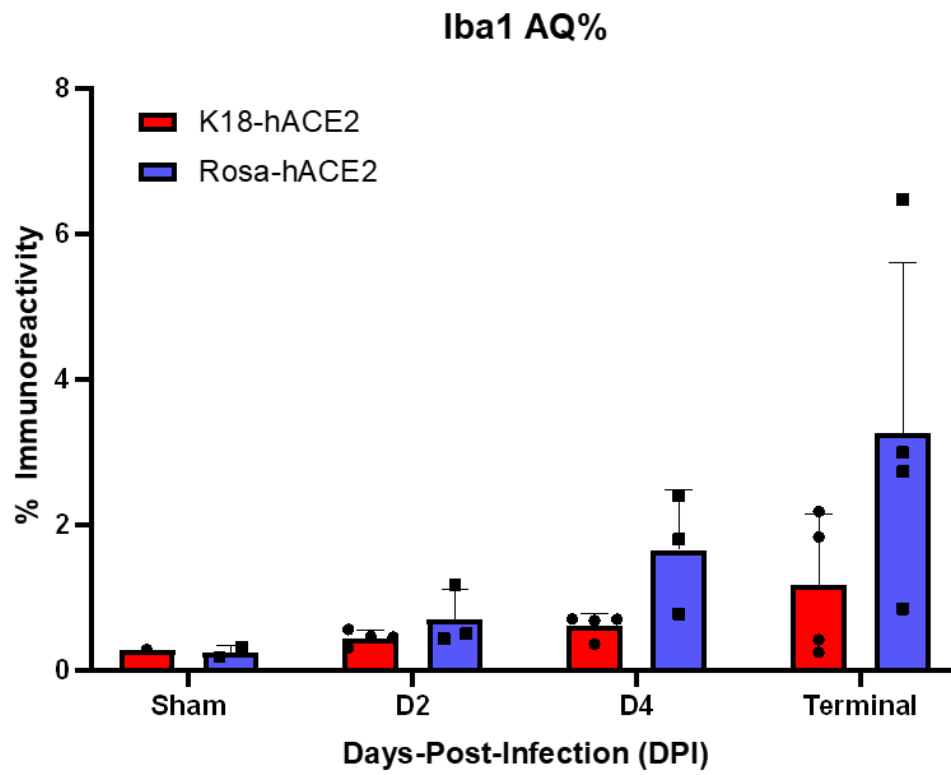
Figure 14: Iba1 AQ% shows increase over the course of infection in both mouse models. This data suggests Rosa26-hACE2 may recruit IBA1+ cells more effectively, but small sample sizes limit the significance.
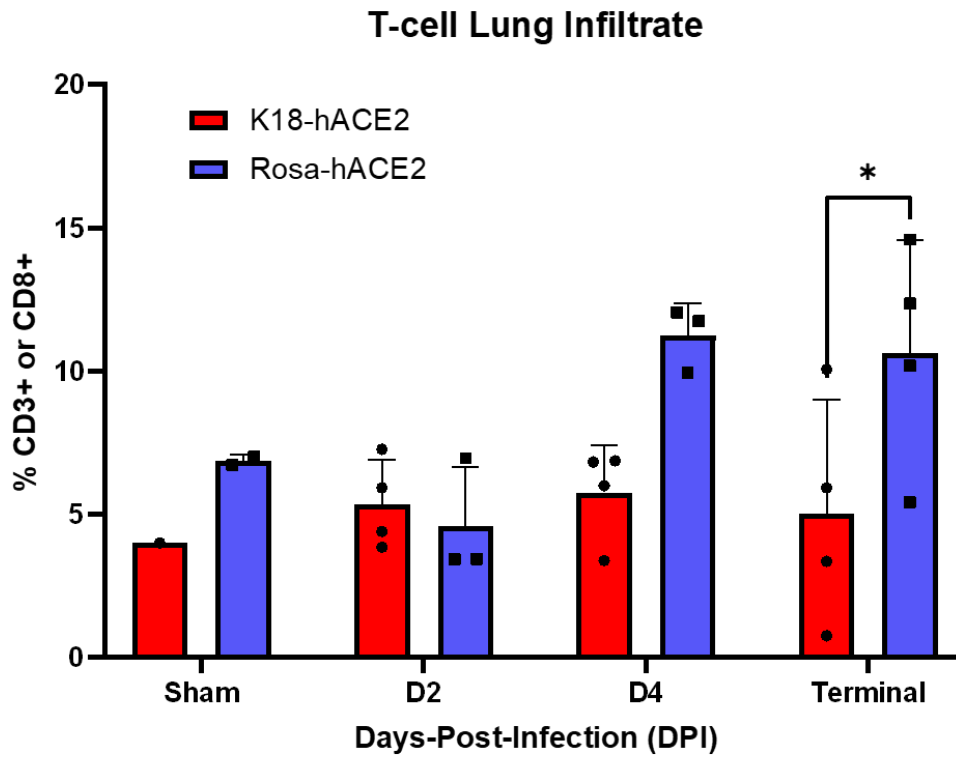
Figure 15: HP of CD3+ or CD8+ cell percentages in both strains shows a significant difference in terminal animals (P = 0.0322). Rosa26-hACE2 T-cells increase over the course of infection, but K18-hACE2 mice do not recruit T-cells as readily.
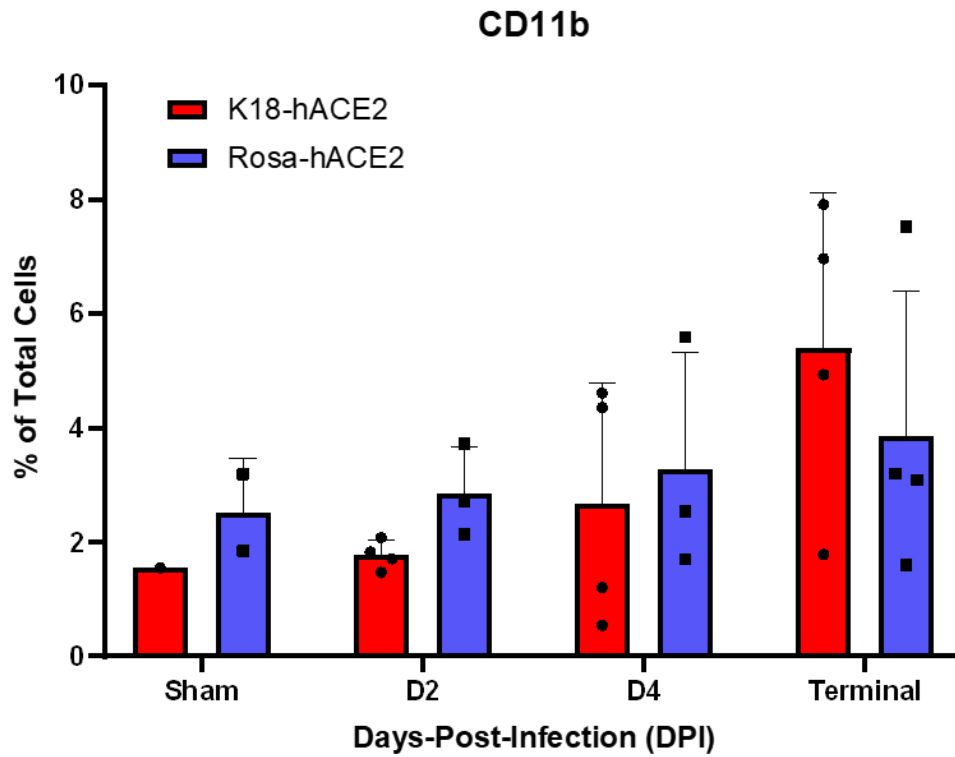
Figure 16: HP of CD11b+ in mIHC panel 1 shows a small increase over the course of infection, but no significant difference is observed between the two transgenic mouse strains.

Histologic distribution of SARS-CoV-2 in K18-hACE2 brain was more diffuse and severe compared to the Rosa26-hACE2 brain.

Sham animals did not show a difference between the two strains in any region of the brain (Figure 17). In terminal animals, brain spike location varied greatly between the two strains, with K18-hACE2 showing severe and widespread by 7 dpi with involvement of the olfactory bulb, as well as of the cerebral cortex (most predominantly somatosensory and somatomotor areas), hippocampus, midbrain (thalamus and hypothalamus), brainstem, and the dentate nucleus (Figure 18). The dentate gyrus was mostly spared. Rosa26-hACE2 showed substantially different patterns of infection, with virus present in ventral portions of the brain including the olfactory bulb, midbrain (thalamus and hypothalamus), and brainstem (Figure 19). Degenerative neurons with swollen cytoplasm or necrotic pyknotic hypereosinophilic neurons, and lymphocytic perivascular cuffing can be observed in both strains of mice. Gliosis is also evident in areas with neuronal injury and minimal delicate mononuclear perivascular cuffing. The cerebellum was spared in both models. Rosa26-hACE2 mice also had much less virus in the brain compared to the K18-hACE2 ($P = 0.0249$) (Figure 20).
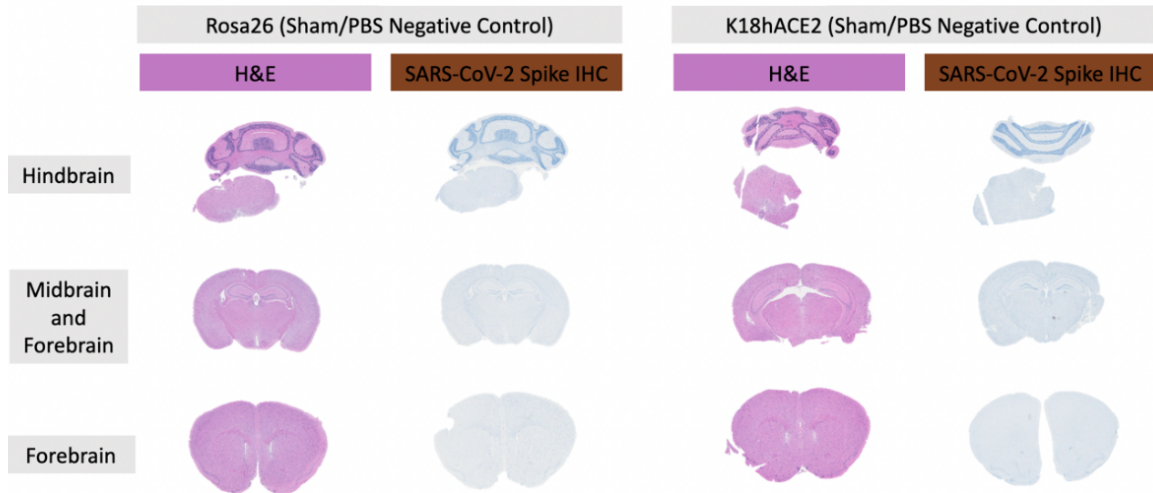
Figure 17: H&E and SARS-CoV-2 spike IHC of Sham K18-hACE2 and Rosa26-hACE2 mice in forebrain, midbrain, and hindbrain. No difference in histology is observed between the two strains in any of the anatomical compartments of the brain, with absence of Spike antigen.
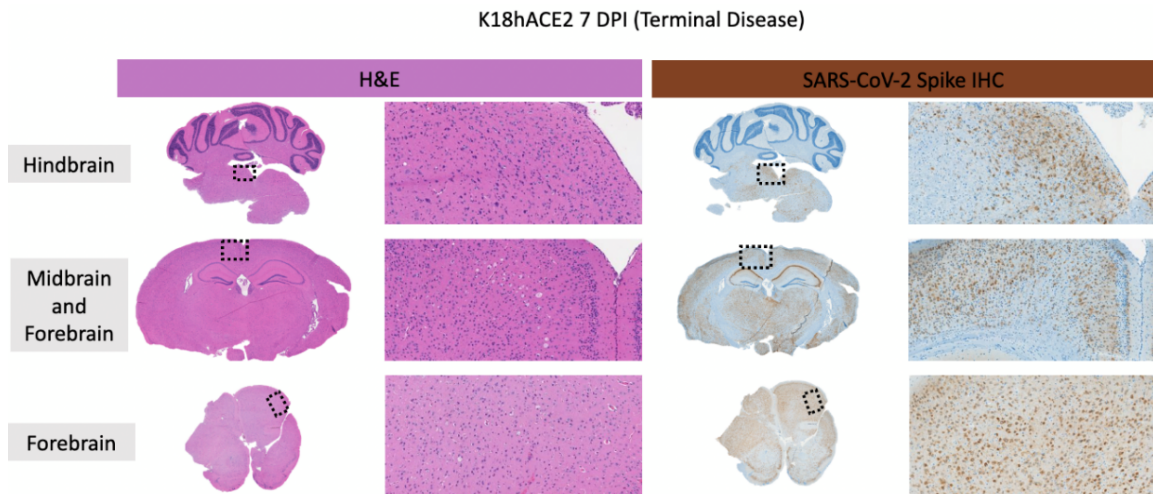
Figure 18: Terminal K18-hACE2 brain showing disseminated viral distribution in forebrain, midbrain, and hindbrain. H&E findings included neuronal degeneration and necrosis as well as gliosis. Spike IHC reveals viral protein throughout the brain, sparing the cerebellum and dentate gyrus, and concentrating in the hippocampus.
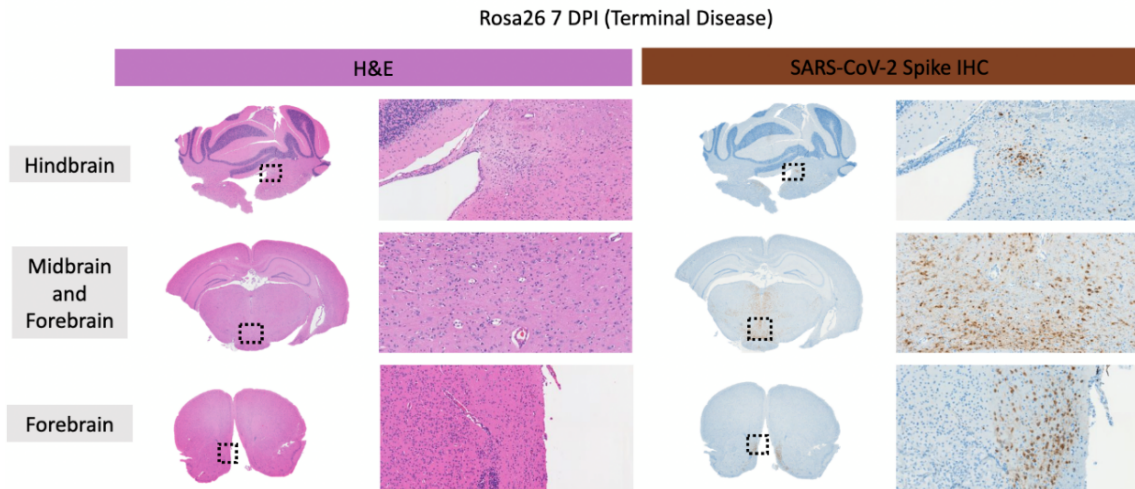
Figure 19: Rosa26-hACE2 terminal brain showing more limited viral antigen distribution. H&E findings included neuronal degeneration, necrosis, as well as gliosis, and spike IHC shows viral proteins in ventral portions of the hindbrain, midbrain, and forebrain.

Coronal Brain Spike+ %
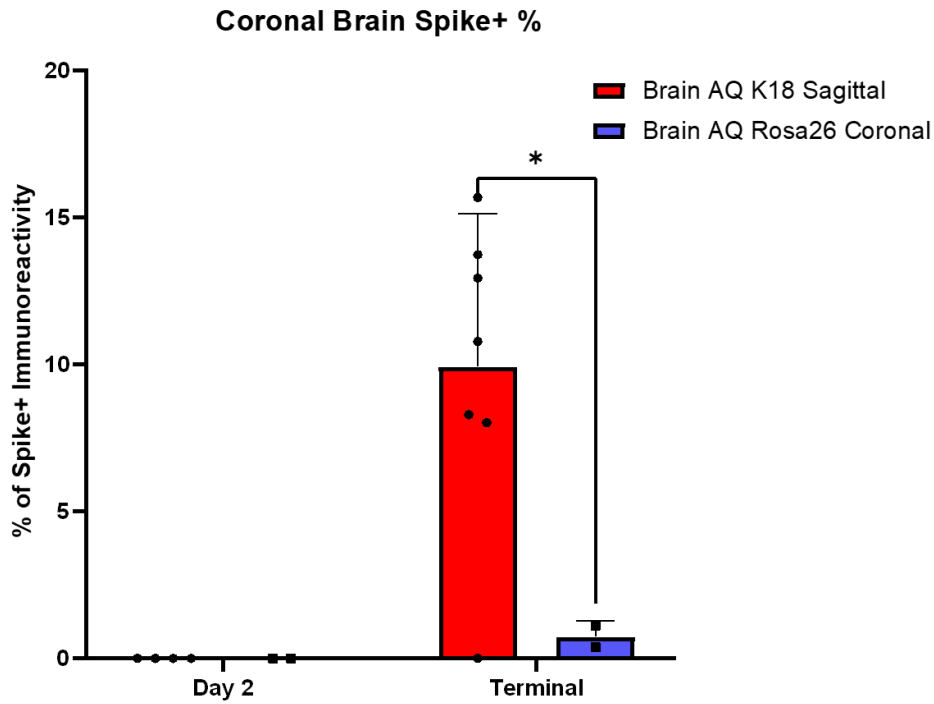
Figure 20: SARS-CoV-2 spike IHC immunoreactivity percentage in both transgenic mouse models. Terminal animals show a statistically significant difference in amount of viral protein (Two-way ANOVA P = 0.0249) reflecting the difference in dissemination within the brain

K18-hACE-2 mice show decreased neuronal density and neuronal death, and reactive microglia in response to infection

By employing the AQ algorithm to quantify immunoreactivity of NeuN, a marker for mature neurons, the total amount of NeuN can be quantified within distinct anatomical compartments. Sham animals show similar amounts of NeuN in all compartments of the midbrain, but terminal animals show a significant decrease in NeuN immunoreactivity in the cortex and hippocampus (Hippocampus $P = 0.0003$, Cortex $P <0.0001$) (Figure 20, 21). The hypothalamus and thalamus regions do not show a significant decrease in NeuN immunoreactivity percentage, perhaps due to the large heterogeneity within the region with NeuN positive cells making up a smaller proportion of the cells within this compartment.

Morphologic aberrations of microglia are also observed in areas with neuronal loss and Spike antigen, with processes expressing IBA1+ more intensely with broader cytoplasmic processes occasionally extending around dead or dying neurons (Figure 21). By using an AQ of IBA1+ immunoreactivity, the differences between sham and terminal animals are shown to be significant in all compartments of the midbrain (Hippocampus $P = 0.0019$, Cortex $P = 0.0005$. Thalamus/hypothalamus $P = 0.0020$) (Figure 22). Although IBA1 readily marks all microglia, it can also mark monocytes migrating in and this makes it impossible to distinguish between the two myeloid-lineage phagocyte populations. Some of the changes associated with terminal K18-hACE2 IBA1+ cells may be partly due to infiltration and differentiation of monocytes; however the absence of significant

perivascular cuffing suggest immune cell recruitment is not playing a major role in

terminal CNS disease.
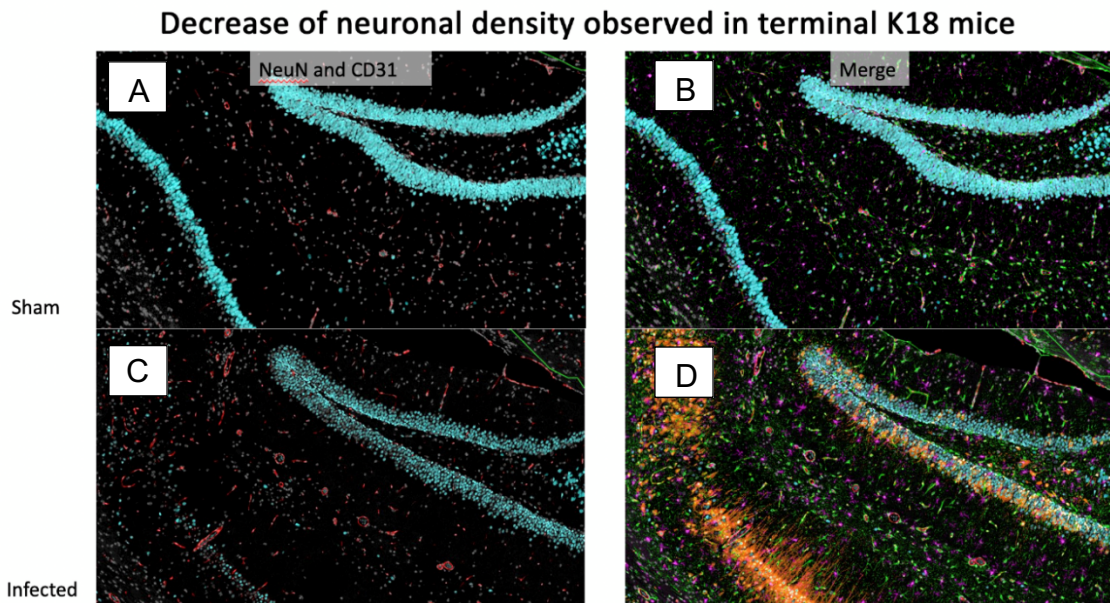
Figure 21: Representative images of the neuronal loss observed in K18-hACE2 terminal animal brains. DAPI – grey, NeuN – teal, GFAP – green, SARS-CoV-2 Spike – Orange, CD31 – Red, IBA1 - Magenta (A) Sham K18-hACE2 in hippocampus showing normal expression of mature neuron marker NeuN with only channels for DAPI, CD31 and NeuN visible. (B) Merge image of all channels of Sham K18-hACE2 in hippocampus. (C) Terminal K18-hACE2 in hippocampus showing decreased expression of mature neuron marker NeuN with channels for DAPI, CD31 and NeuN visible. (D) Merged image of all channels of image C.
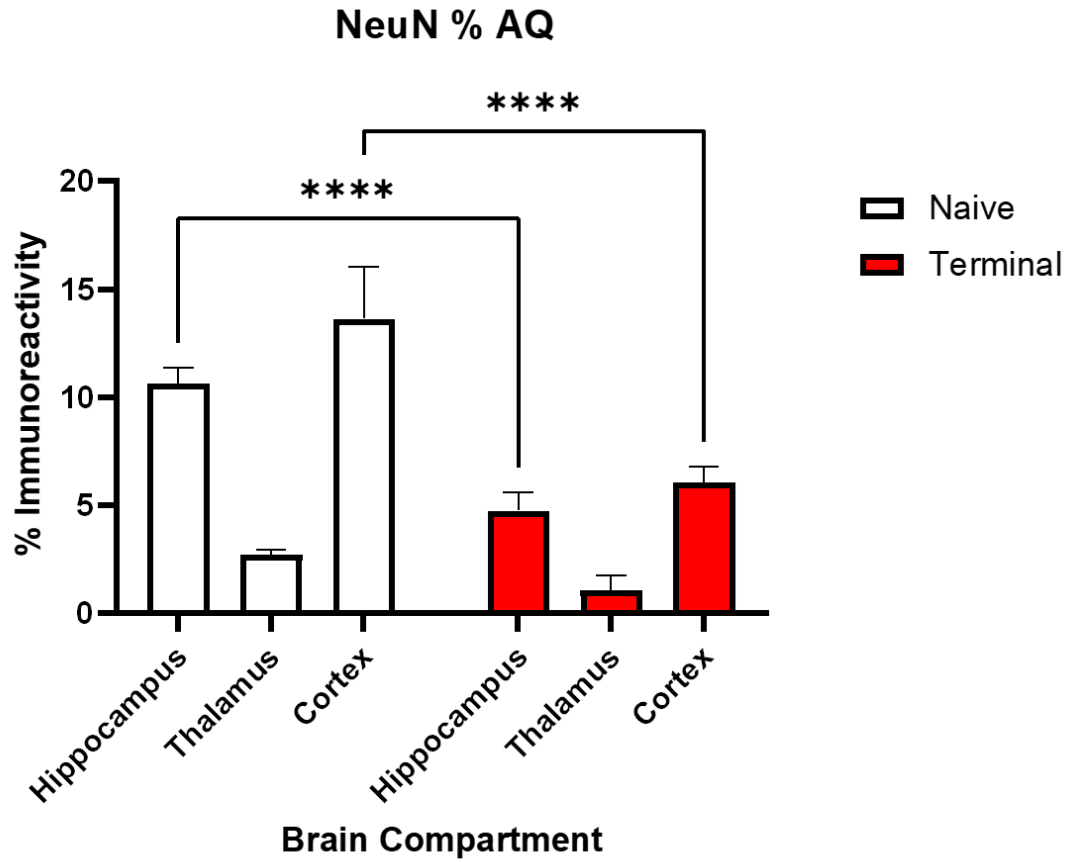
Figure 22: NeuN AQ immunoreactivity percentage in different midbrain components of both naïve and terminal K18-hACE2 animals. Hippocampus and cortex show significant decrease in NeuN immunoreactivity between sham and terminal animals (Hippocampus P = 0.0003, Cortex P <0.0001)
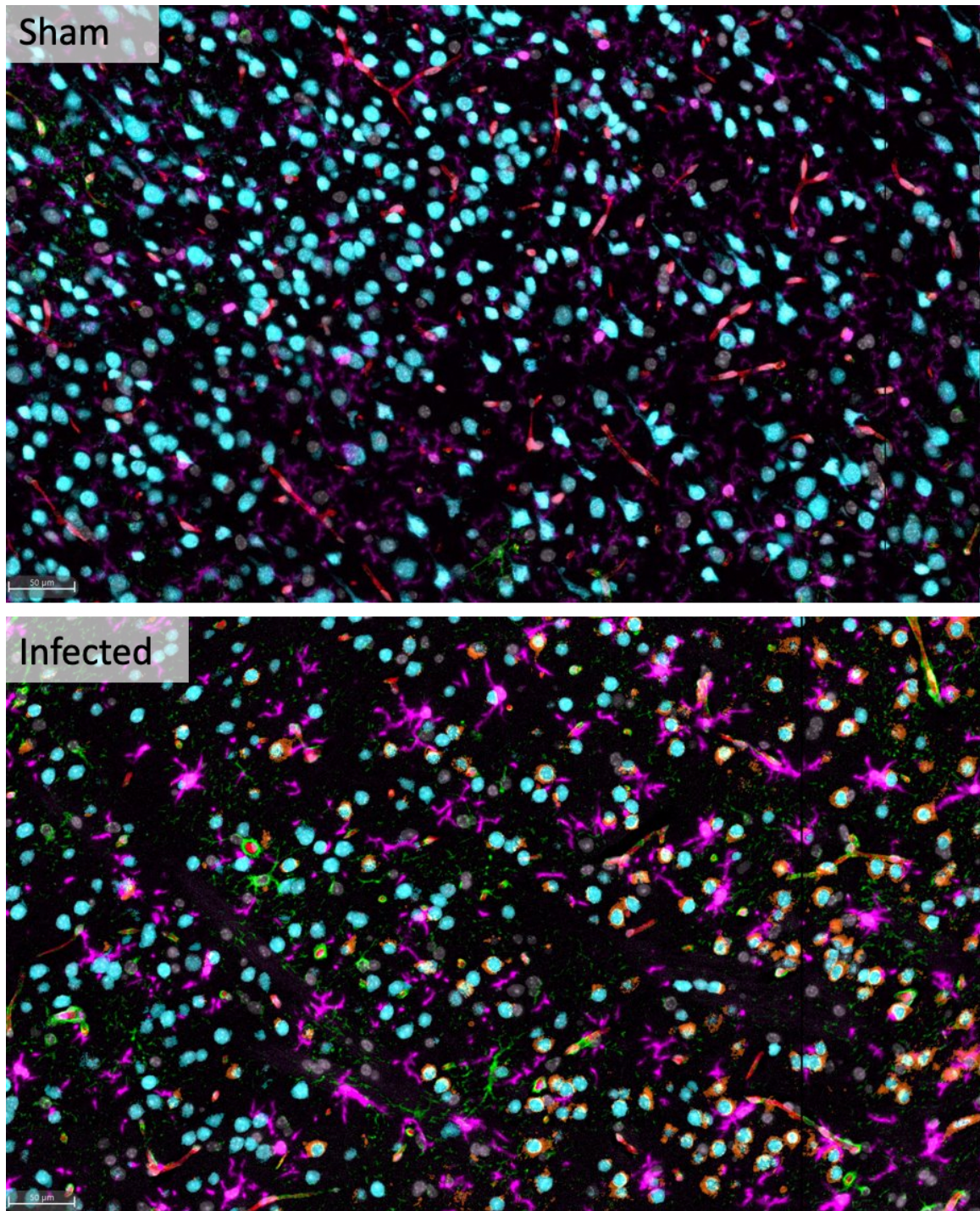
Figure 23: Reactive microglia (IBA1+) observed in terminal K18-hACE2 midbrain when compared to sham K18-hACE2 midbrain. DAPI – grey, NeuN – teal, GFAP – green, SARS-CoV-2 Spike – Orange, CD31 – Red, IBA1 – Magenta

Figure 24: IBA1+ AQ in various compartments of the midbrain in sham and terminal K18-SARS-CoV-2 mice. All compartments showed a significant difference in IBA1+ immunoreactivity between sham and infected mice (Hippocampus P = 0.0019, Cortex P = 0.0005. Thalamus/hypothalamus P = 0.0020)

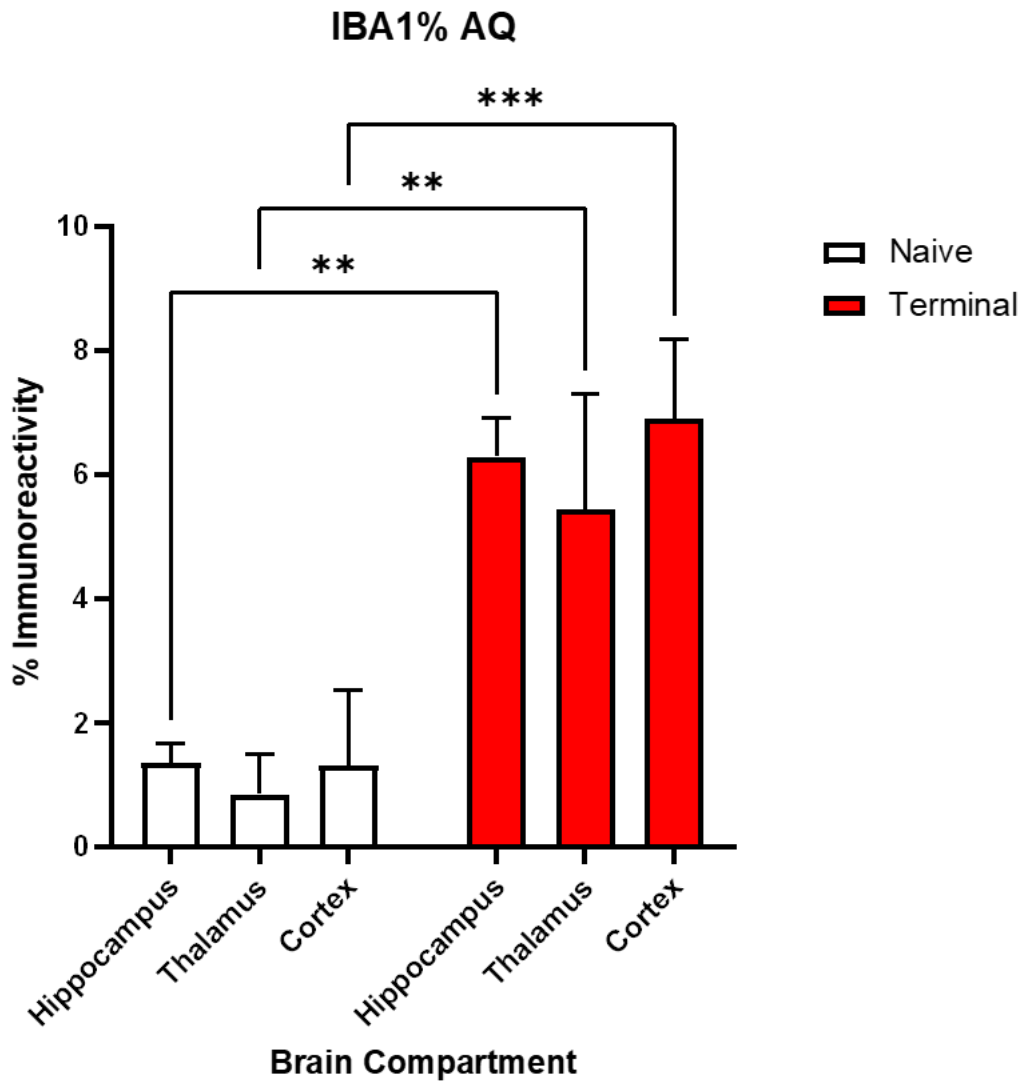| ID	Strain	Dose	DPI	Brain processing	Terminal temperature	Neuroinvasion-Brain (+/-)	Nasal passage Spike IHC	Lung Spike IHC	Severity of pneumonia	Lung Ordinal Score	Brain Spike IHC
657	Rosa26	1.00E+05	5	Sagittal	35.6	+	1	1	Moderate to regionally marke	5	2
661	Rosa26	1.00E+05	8	Sagittal	27.8	+	1	1	Moderate	4	1
749	Rosa26	1.00E+05	2	Sagittal	36.9	-	3	1	Within normal limits	0	0
750	Rosa26	1.00E+05	2	Sagittal	37.5	-	2	1	Minimal	1	0
752	Rosa26	1.00E+05	4	Sagittal	34.9	-	Unk	2	Mild to moderate	3	0
756	Rosa26	1.00E+05	4	Sagittal	36.2	-	1	2	Moderate	4	0
757	Rosa26	1.00E+05	4	Sagittal	36.4	-	1	2	Mild	2	0
760	Rosa26	1.00E+05	7	Sagittal	35.1	-	1	1	Moderate to regionally marke	5	0
761	Rosa26	1.00E+05	7	Sagittal	37.4	-	0	0	Minimal	1	0
765	Rosa26	1.00E+05	2	Sagittal	33.7	-	1	0	Within normal limits	0	0
770	Rosa26	1.00E+05	7	Sagittal	32.5	+	1	2	Mild	2	2
1159	K18hACE2	1.00E+05	2	Sagittal	36.9	-	2	2	Minimal to mild	2	0
1160	K18hACE2	1.00E+05	4	Sagittal	36.4	-	0	1	Mnimal to mild	2	0
1163	K18hACE2	1.00E+05	7	Sagittal	25	+	0	1	Minimal	1	3
1168	K18hACE2	1.00E+05	7	Sagittal	25.9	+	1	2	Moderate to regionally marke	5	3
1169	K18hACE2	1.00E+05	8	Sagittal	37.5	+	1	3	Mild to moderate	3	3
1172	K18hACE2	1.00E+05	2	Sagittal	34.3	-	2	2	Minimal	1	0
1173	K18hACE2	1.00E+05	4	Sagittal	35.5	-	0	0	Within normal limits	0	0
1176	K18hACE2	1.00E+05	7	Sagittal	25.2	+	1	0	Within normal limits	0	3
1342	K18hACE2	1.00E+05	7	Sagittal	25	+	1	3	Mild	2	3
1345	K18hACE2	1.00E+05	7	Sagittal	25	+	1	3	Mild	2	3
1655	K18hACE2	1.00E+05	2	coronal brain	37	-	3	2	Minimal	1	0
1656	K18hACE2	1.00E+05	2	coronal brain	35.8	-	2	3	Mild to moderate	3	0
1661	K18hACE2	1.00E+05	4	coronal brain	37.4	+	1	3	Mild to moderate	3	1
1662	K18hACE2	1.00E+05	4	coronal brain	37.3	-	2	3	Moderate	4	0
1664	K18hACE2	1.00E+05	4	coronal brain	37.5	+	2	3	Moderate	4	2
1667	K18hACE2	1.00E+05	4	coronal brain	37.1	-	3	1	Minimal	1	0
1757	K18hACE2	1.00E+05	7	coronal brain	25	+	0	3	Minimal	1	3
1758	K18hACE2	1.00E+05	7	coronal brain	25.3	+	0	3	Mild	2	3
1771	K18hACE2	1.00E+05	8	coronal brain	25	+	1	1	Minimal	1	3
1781	K18hACE2	1.00E+05	7	coronal brain	36.1	-	0	1	Mild to moderate	3	0
1782	K18hACE2	1.00E+05	8	coronal brain	25	+	1	2	Mild	2	3
1784	K18hACE2	1.00E+05	7	coronal brain	25.1	+	1	2	Within normal limits	0	3
1791	Rosa26	1.00E+05	8	coronal brain	25.9	+	2	2	Moderate	4	2
1794	Rosa26	1.00E+05	8	coronal brain	32.7	+	2	2	Moderate to regionally marke	5	2
1802	Rosa26	1.00E+05	7	coronal brain	25.2	+	1	2	Moderate to regionally marke	5	2
1803	Rosa26	1.00E+05	7	coronal brain	25	+	2	2	Moderate	4	2

Table 4. Tg-mice individual animal histopathology summary data.

DISCUSSION

As evident by this study and others, K18-hACE2 readily succumb to SARS-CoV-2 infection and the usage of this model is widespread in SARS-CoV-2 research for this reason. However, as shown by temporal virological, molecular, and spike immunoreactivity in lung and brain, as well as the mild nature of lung pathology, mortality is attributable to neurodissemination. Furthermore, histological findings in the lungs do not demonstrate hallmarks of DAD, and most of the lung parenchyma remains normal throughout infection. Since CD11b+ IBA1- cells do not play a large role in the lung infiltrate of this model, this suggests the neutrophilic bystander damage seen in severe SARS-CoV-2 disease is not present in this model either. None of the K18-hACE2 mice within this study developed what could be considered severe pneumonia, with all mice showing less than 5% of the lung parenchyma to be consolidated. Mice also did not show any typical signs of a respiratory disease, such as nasal discharge, wheezing, and open mouth breathing. Instead, the viral neuroinvasion that is observed as early as day 4 with subsequent neurodissemination in terminal disease should be regarded as the cause of death in this model. Clinical signs in K18-hACE2 mice such as neurological signs including tremors, irresponsiveness, and hypothermia can be attributable to neuronal injury and death observed histologically. These clinical signs can also be linked to ultrastructural findings that corresponds with peak viral load in the brain, with simultaneous low to undetectable levels in the lung. Since viral spike protein is first observed in the olfactory bulb of K18-hACE2 brains and the olfactory epithelium, this suggests that the virus is likely entering the brain via axonal processes extending through

the cribriform plate. Since this model has been utilized in numerous studies with more preprint literature suggesting the usage of this model is not slowing, there are severe implications with the results of these studies. An obvious flaw with this model would be the numerous therapeutics and vaccines tested that show no efficacy, simply because the disease progression is significantly different from humans and these drugs are not created to prevent neuroinvasion and dissemination. Furthermore, studies published in high impact journals reporting severe lung disease as a finding with the K18-hACE2 model have made any opposition difficult to put out into literature.

The Rosa26-hACE2 model did not show as severe neurological signs as the K18-hACE2, with many animals continuing to remain ambulatory without motor dysfunction, which is congruent with the more limited viral infection within the brain. The pathway for viral entry into the Rosa26-hACE2 mouse model is even less clear since virus is first seen in the midbrain as well as the olfactory bulb, suggesting an alternate route than what is seen in the K18-hACE2. Despite the ACE2 IHC and RNAscope® ISH data showing comparable expression of *hACE2* in the olfactory epithelium in both strains, the mechanism of action in Rosa26-hACE2 for viral transport to the brain is likely via olfactory neural epithelium, but other routes should be considered, including axonal transport from cranial nerves. The ACE2 IHC and RNAscope® ISH data also show absence of *hACE2* expression within AT1 cells, although spike IHC reveals these cell types to have viral antigen. Dissemination within the brain is also ACE2-independent as many neurons were not shown to express ACE2. These findings suggest a host factor that allows for ACE2 independent infection of many cell types and that ACE2 expression is

not the only requirement for ACE2-dependent infection. Other cofactors, such as Neuropilin 1, have been described as a receptor for viral entry, and it has been proposed that sugar molecules and the sialic acids N-glycolylneuraminic acid, N-acetylneuraminic acid, and their derivates may also allow viral entry [78].

Another clear difference between the two strains besides the contrast in viral brain dissemination patterns is the more robust lung immune infiltrate, despite the similar hACE2 expression within lung parenchyma. The more specific insertion location in the Rosa26-hACE2 mouse could have avoided disrupting important host immune response gene expression, or an important cofactor for preventing viral entry and replication, since the Rosa26 locus does not affect any genes downstream unlike the random insertion of the K18-hACE2 model. Additionally, it is interesting to note that despite having eight copies of the transgene compared to the Rosa26-hACE2's single copy, the K18-ACE2 still shows similar levels of hACE2 expression, but the reasons for this discrepancy remain unclear. qPCR may be a better tool as it is more sensitive than IHC and RNAscope® ISH. No genes are annotated in the region of insertion in the K18-hACE2 model currently, but the differences described in this study clearly show a difference that could only be a result of the insertion locations.

Relevance to human SARS-CoV-2 neuroinvasion is likely limited, as neuroinvasion in humans has limited evidence, with isolated case reports describing rapid mood swings preceding a positive COVID-19 test and declining clinical findings [79]. Common clinical features of even mild SARS-CoV-2 infection include a stark loss in smell and

taste in more than half of cases, suggesting involvement of olfactory neurons, which exist

in the nasal epithelium. This site has been showed to be affected by SARS-CoV-2

infection. Numerous papers describe viral RNA found within the brain, as well as some

evidence of microinfarcts and viral spike protein found in the brain in case study reports.

However, after almost a half billion cases globally, the limited number of potential

encephalopathy cases suggests neuroinvasion of the virus is exceedingly rare at most, and

the K18-hACE2 has very limited translational ability for SARS-CoV-2 neurological

consequences. Brain organoids have demonstrated to be susceptible to SARS-CoV-2

infection, but when ACE2 is blocked, no infection occurs [80]. This contradicts the

ACE2 independent manner viral dissemination occurs in the tg mouse models, as many

neurons and AT1 cells did not express ACE2 detectable by IHC or RNAscope® ISH. No

type I interferon response was detected either, which could be due to the organoid's

inability to fully recapitulate the complexities of interorgan communication and the

immune system, but the lack of immune response within both tg mouse models does

corroborate this lack of host response.

The role of reactive microglia observed in K18-hACE2 mice remains unclear, but

microglia play an important role in all encephalitis by sensing a wide variety of stimuli

and coordinating the innate and adaptive immune response. Resting state microglia have

a high degree of mobility by using processes and protrusions to patrol the brain

parenchyma. However, during encephalitis, several microglial proteins have been

implicated in promoting viral replication including Peli1, which is a type 1 interferon

antagonist. STAT1 has been implicated as regulating microglia-mediated synaptic

stripping and further neuronal damage, but SARS-CoV-2 protein ORF6 has been shown to block STAT1 translocation to the nucleus for signal transduction [81]. IBA1+ also is not specific to microglia and can mark monocytes that may be migrating in in response to the infection. It would be beneficial to add Rosa26-hACE2 brains to the mIHC panel 2 to see if there is also a loss of neuronal density in areas of high viral replication, as well as evaluate changes in microglia. Since there is more efficient recruitment of infiltrate to lungs, perhaps Rosa26-hACE2 mice may have a more robust response in the brain. Adding brains from day 2 and 4 mice to the mIHC panel 2 data would also be of benefit, as to determine if microglia activation begins after neuronal density is already declining or if elevated cytokines within the blood in response to lung pathology are responsible for the morphological changes of the microglia before virus reaches the brain.

Using the Rosa26-hACE2 and K18-hACE2 brains, spatial transcriptomics with 10X Genomics (Pleasanton, CA) on the FFPE tissue is ongoing. This will hopefully shed some light on the complexities occurring with the host immune response and why little immune infiltrate is observed in K18-hACE2 brains. Some transcripts of particular interest would be pathways relating to Type I interferon response including stimulator of interferon genes (STING), MHC I and II presentation, and apoptosis suppression.

Data from this study only adds additional layers to the seemingly endless intricacies of infectious disease and host-pathogen interactions. Although much caution must be taken when using the hACE2-expressing transgenic mouse models in regard to the severe neuroinvasion that is the main factor of lethality, these transgenic models are not without

their benefits, as there is still translational potential for lung disease and host immune response, and termination before neuroinvasion can occur on day 4 may avoid the confounding effects of encephalopathy. These models would be ideal for studying protective factors of immune systems as well as host receptors necessary for viral entry, as viral tropism has been shown to be partly ACE2 independent. Mechanisms governing viral neuroinvasion could also be further examined using the K18-hACE2 model, as well as host responses that contribute to damage within the brain. Further characterization of the location the K18-hACE2 cassette was inserted into the K18-hACE2 mouse could allow further explanation for the differences between the two strains too, and a more complete understanding of factors that affect viral susceptibility.

Although data from this study was not able to support using these transgenic models as the much-needed model for severe SARS-CoV-2 disease, the characterization and data will hopefully guide other research groups to use these models in an appropriate manner. Moreover, this study demonstrates the multidisciplinary team effort needed for a more complete picture of any aspect in infectious disease and immunology. Techniques and expertise in molecular basic science, animal models, pathology, and immunology were all necessary to generate layers of data that tell a more complete story, and fostered innovation and problem solving. The scientific community benefits from these types of teams, as it provides more conclusive data by having insights from multiple perspectives. By combining expertise and resources, bigger and more complex scientific questions can be investigated in greater depth, and each collaborator walks away with a deeper understanding of research from other disciplines.

REFERENCES

[1] Center for Systems Science and Engineering at Johns Hopkins University. (n.d.).
COVID-19 Dashboard. ArcGIS dashboards. Retrieved March 1, 2022, from
https://gisanddata.maps.arcgis.com/apps/dashboards/bda7594740fd40299423467b
48e9ecf6

[2] Morens, D. M., Daszak, P., Markel, H., & Taubenberger, J. K. (2020). Pandemic
COVID-19 Joins History's Pandemic Legion. *mBio*, *11*(3), e00812–20.
https://doi.org/10.1128/mBio.00812-20

[3] Covid-19 fueling Anti-Asian racism and xenophobia worldwide. *Human Rights
Watch*. (2020, October 28). Retrieved March 1, 2022, from
https://www.hrw.org/news/2020/05/12/covid-19-fueling-anti-asian-racism-and-
xenophobia-worldwide

[4] Fiorillo, V. (2021, October 16). School masks are now a "satanic ritual," according to
parents suing a local school district. *Philadelphia Magazine*. Retrieved March 1,
2022, from https://www.phillymag.com/news/2021/10/15/school-mask-mandate-
lawsuit-bucks-county/

[5] El Zowalaty, M. E., & Järhult, J. D. (2020). From SARS to COVID-19: A previously
unknown SARS- related coronavirus (SARS-CoV-2) of pandemic potential
infecting humans – Call for a One Health approach. *One Health*, *9*, 100124–
100124. https://doi.org/10.1016/j.onehlt.2020.100124

[6] Drosten, C., Günther, S., Preiser, W., van der Werf, S., Brodt, H.-R., Becker, S.,
Rabenau, H., Panning, M., Kolesnikova, L., Fouchier, R. A. ., Berger, A.,
Burguière, A.-M., Cinatl, J., Eickmann, M., Escriou, N., Grywna, K., Kramme, S.,
Manuguerra, J.-C., Müller, S., … Doerr, H. W. (2003). Identification of a Novel
Coronavirus in Patients with Severe Acute Respiratory Syndrome. *The New
England Journal of Medicine*, *348*(20), 1967–1976.
https://doi.org/10.1056/NEJMoa030747

[7] Memish, Z. (2016). MERS. *International Journal of Infectious Diseases*, *53*, 23–23.
https://doi.org/10.1016/j.ijid.2016.11.061

[8] Banerjee A, Subudhi S, Rapin N, Lew J, Jain R, Falzarano D, et al. (2020). Selection
of viral variants during persistent infection of insectivorous bat cells with Middle
east respiratory syndrome coronavirus. *Scientific Reports, 10*, 1–15. doi:
10.1038/s41598-020-64264-1

[9] Haagmans BL, van den Brand JM, Raj VS, Volz A, Wohlsein P, Smits SL, et al.
(2016) An orthopoxvirus-based vaccine reduces virus excretion after MERS-CoV

infection in dromedary camels. *Science*, *351,* 77–81. doi: 10.1126/science.aad1283

[10] Choo, S. W., Zhou, J., Tian, X., Zhang, S., Qiang, S., O'Brien, S. J., Tan, K. Y., Platto, S., Koepfli, K., Antunes, A., & Sitam, F. T. (2020). Are pangolins scapegoats of the COVID-19 outbreak-CoV transmission and pathology evidence? *Conservation Letters*, *13*(6), e12754. https://doi.org/10.1111/conl.12754

[11] Alluwaimi, A. M., Alshubaith, I. H., Al-Ali, A. M., & Abohelaika, S. (2020). The Coronaviruses of Animals and Birds: Their Zoonosis, Vaccines, and Models for SARS-CoV and SARS-CoV2. *Frontiers in Veterinary Science*, *7*, 582287– 582287. https://doi.org/10.3389/fvets.2020.582287

[12] Cai, H. Y., & Cai, A. (2021). SARS-CoV2 spike protein gene variants with N501T and G142D mutation–dominated infections in mink in the United States. *Journal of Veterinary Diagnostic Investigation*, *33*(5), 939–942. https://doi.org/10.1177/10406387211023481

[13] Hedman, H. D., Krawczyk, E., Helmy, Y. A., Zhang, L., & Varga, C. (2021). Host Diversity and Potential Transmission Pathways of SARS-CoV-2 at the Human- Animal Interface. *Pathogens*, *10*(2), 180. https://doi.org/10.3390/pathogens10020180

[14] Mallapaty, S., Maxmen, A., & Callaway, E. (2021). 'Major stones unturned': COVID origin search must continue after WHO report, say scientists. *Nature*, *590*(7846), 371–372. https://doi.org/10.1038/d41586-021-00375-7

[15] Guo, H. (2020, January 22). *Snakes could be the original source of the new coronavirus outbreak in China*. Scientific American. Retrieved March 28, 2022, from https://www.scientificamerican.com/article/snakes-could-be-the-original- source-of-the-new-coronavirus-outbreak-in-china/

[16] Greenberg, A. (2021, March 5). What's the deal with Mink Covid? *PBS*. Retrieved March 1, 2022, from https://www.pbs.org/wgbh/nova/article/mink-covid-virus- mutation/

[17] NBCUniversal News Group. (2020, December 2). Here's why Denmark culled 17 million minks and now plans to dig up their buried bodies. The Covid Mink Crisis, explained. *NBCNews.com*. Retrieved March 28, 2022, from https://www.nbcnews.com/news/animal-news/here-s-why-denmark-culled-17- million-minks-now-plans-n1249610

[18] Reardon, S. (2021, September 27). Do monoclonal antibodies help COVID patients? *Scientific American*. Retrieved March 1, 2022, from

https://www.scientificamerican.com/article/do-monoclonal-antibodies-help-covid-patients/

[19] Mohammadi, M., Shayestehpour, M., & Mirzaei, H. (2021). The impact of spike mutated variants of SARS-CoV2 [Alpha, Beta, Gamma, Delta, and Lambda] on the efficacy of subunit recombinant vaccines. *The Brazilian Journal of Infectious Diseases*, *25*(4), 101606–101606. https://doi.org/10.1016/j.bjid.2021.101606

[20] Koyama, T., Platt, D., & Parida, L. (2020). Variant analysis of SARS-CoV-2 genomes. *Bulletin of the World Health Organization*, *98*(7), 495–504. https://doi.org/10.2471/BLT.20.253591

[21] SIB Swiss Institute of Bioinformatics | Disclaimer. (n.d.). Coronaviridae. *ViralZone*. Retrieved March 1, 2022, from https://viralzone.expasy.org/30?outline=all_by_species

[22] "Phylogeny of SARS-like betacoronaviruses". *nextstrain*. Retrieved 18 January 2020.

[23] Memish, Z. A.; Zumla, A. I.; Al-Hakeem, R. F.; Al-Rabeeah, A. A.; Stephens, G. M. (2013). Family Cluster of Middle East Respiratory Syndrome Coronavirus Infections. *New England Journal of Medicine*, *368*(26), 2487–2494. doi:10.1056/NEJMoa1303729. PMID 23718156.

[24] Astuti, I., & Ysrafil. (2020). Severe Acute Respiratory Syndrome Coronavirus 2 (SARS-CoV-2): An overview of viral structure and host response. *Diabetes & Metabolic Syndrome: Clinical Research & Reviews*, *14*(4), 407–412. https://doi.org/10.1016/j.dsx.2020.04.020

[25] Bayati, A., Kumar, R., Francis, V., & McPherson, P. S. (2021). SARS-CoV-2 infects cells after viral entry via clathrin-mediated endocytosis. *The Journal of Biological Chemistry*, *296*, 100306–100306. https://doi.org/10.1016/j.jbc.2021.100306

[26] Chakraborty, S. (2021). Evolutionary and structural analysis elucidates mutations on SARS-CoV2 spike protein with altered human ACE2 binding affinity. *Biochemical and Biophysical Research Communications*, *534,* 374–380. https://doi.org/10.1016/j.bbrc.2020.11.075

[27] McBride, R., van Zyl, M., & Fielding, B. C. (2014). The Coronavirus Nucleocapsid Is a Multifunctional Protein. *Viruses*, *6*(8), 2991–3018. https://doi.org/10.3390/v6082991

[28] Xu X, Chen P, Wang J, Feng J, Zhou H, Li X, et al. (March 2020). "Evolution of the novel coronavirus from the ongoing Wuhan outbreak and modeling of its spike

protein for risk of human transmission". *Science China. Life Sciences*, *63*(3), 457–460. doi:10.1007/s11427-020-1637-5. PMC 7089049. PMID 32009228.

[29] Hoffmann M, Kleine-Weber H, Schroeder S, Krüger N, Herrler T, Erichsen S, et al. (April 2020). "SARS-CoV-2 Cell Entry Depends on ACE2 and TMPRSS2 and Is Blocked by a Clinically Proven Protease Inhibitor". *Cell, 181*(2): 271–280.e8. doi:10.1016/j.cell.2020.02.052. PMC 7102627. PMID 32142651.

[30] Aronson JK (25 March 2020). "Coronaviruses – a general introduction". *Centre for Evidence-Based Medicine, Nuffield Department of Primary Care Health Sciences, University of Oxford*. Archived from the original on 22 May 2020. Retrieved 24 May 2020

[31] Örd, M., Faustova, I., & Loog, M. (2020). The sequence at Spike S1/S2 site enables cleavage by furin and phospho-regulation in SARS-CoV2 but not in SARS-CoV1 or MERS-CoV. *Scientific Reports*, *10*(1), 16944–16944. https://doi.org/10.1038/s41598-020-74101-0

[32] Kaur, G., Sharma, S., & Rahman, I. (2020). Dysregulated ACE2 and Furin Activity amongst Smokers Increase Disease Susceptibility Towards SARS-CoV2. *Free Radical Biology & Medicine*, *159*, S80–S81. https://doi.org/10.1016/j.freeradbiomed.2020.10.210

[33] Graier, T., Golob-Schwarzl, N., Weger, W., Benezeder, T., Painsi, C., Salmhofer, W., & Wolf, P. (2021). Furin Expression in Patients With Psoriasis-A Patient Cohort Endangered to SARS-COV2? *Frontiers in Medicine*, *8*, 624462–624462. https://doi.org/10.3389/fmed.2021.624462

[34] Zamorano Cuervo N, Grandvaux N (November 2020). ACE2: Evidence of role as entry receptor for SARS-CoV-2 and implications in comorbidities. *eLife*. *9*. doi:10.7554/eLife.61390

[35] Wang K, Chen W, Zhang Z, Deng Y, Lian JQ, Du P, et al. (December 2020). "CD147-spike protein is a novel route for SARS-CoV-2 infection to host cells". *Signal Transduction and Targeted Therapy*, *5*(1), 283. bioRxiv 10.1101/2020.03.14.988345. https://doi.org/10.1038/s41392-020-00426-x

[36] Weingarten-Gabbay S, Klaeger S, Sarkizova S, Pearlman LR, Chen DY, Bauer MR, Taylor HB, Conway HL, Tomkins-Tinch CH, Finkel Y, Nachshon A, Gentili M, Rivera KD, Keskin DB, Rice CM, Clauser KR, Hacohen N, Carr SA, Abelin JG, Saeed M, Sabeti PC. SARS-CoV-2 infected cells present HLA-I peptides from canonical and out-of-frame ORFs. *bioRxiv* [Preprint]. 2020 Oct 26:2020.10.02.324145. doi: 10.1101/2020.10.02.324145. PMID: 33024965; PMCID: PMC7536868.

[37] Konno Y, Kimura I, Uriu K, Fukushi M, Irie T, Koyanagi Y, et al. SARS-CoV-2 ORF3b Is a Potent Interferon Antagonist Whose Activity Is Increased by a Naturally Occurring Elongation Variant. *Cell Reports* (2020) 32(12):108185. doi: 10.1016/j.celrep.2020.108185

[38] Miorin L, Kehrer T, Sanchez-Aparicio MT, Zhang K, Cohen P, Patel RS, et al. (2020). SARS-CoV-2 Orf6 Hijacks Nup98 to Block STAT Nuclear Import and Antagonize Interferon Signaling. *Proceedings of the National Academy of Sciences of the United States of America*, *117*(45), 28344–28354. doi: 10.1073/pnas.2016650117

[39] Cao Z, Xia H, Rajsbaum R, Xia X, Wang H, Shi PY (2021). Ubiquitination of SARS-CoV-2 ORF7a Promotes Antagonism of Interferon Response. *Cellular & Molecular Immunology*, *18*, 746–748. doi: 10.1038/s41423-020-00603-6

[40] Lei X, Dong X, Ma R, Wang W, Xiao X, Tian Z, et al. (2020). Activation and Evasion of Type I Interferon Responses by SARS-CoV-2. *Nature Communications*, *11*(1), 3810. doi: 10.1038/s41467-020-17665-9

[41] Issa E, Merhi G, Panossian B, Salloum T, Tokajian S. (2020). SARS-CoV-2 and ORF3a: Nonsynonymous Mutations, Functional Domains, and Viral Pathogenesis. *mSystems, 5*(3), e00266–20. doi: 10.1128/mSystems.00266-20

[42] Freundt EC, Yu L, Goldsmith CS, Welsh S, Cheng A, Yount B, et al. (2010). The Open Reading Frame 3a Protein of Severe Acute Respiratory Syndrome-Associated Coronavirus Promotes Membrane Rearrangement and Cell Death. *Journal of Virology*, *84*(2), 1097–109. doi: 10.1128/JVI.01662-09

[43] Azad GK, Khan PK. (2021). Variations in Orf3a Protein of SARS-CoV-2 Alter its Structure and Function. *Biochemistry and Biophysics Reports*, *26,* 100933. doi: 10.1016/j.bbrep.2021.100933

[44] Shi CS, Qi HY, Boularan C, Huang NN, Abu-Asab M, Shelhamer JH, et al. (2014). SARS-Coronavirus Open Reading Frame-9b Suppresses Innate Immunity by Targeting Mitochondria and the MAVS/TRAF3/TRAF6 Signalosome. *Journal of Immunology*, *193*(6), 3080–3089. doi: 10.4049/jimmunol.1303196

[45] Klein S, Cortese M, Winter SL, et al. SARS-CoV-2 structure and replication characterized by in situ cryo-electron tomography. bioRxiv. 2020. 10.1101/2020.06.23.167064.

[46] Wen, Z., Zhang, Y., Lin, Z., Shi, K., & Jiu, Y. (2021). Cytoskeleton—a crucial key in host cell for coronavirus infection. *Journal of Molecular Cell Biology, 12*(12), 968-979. https://doi.org/10.1093/jmcb/mjaa042

[47] De Haan, C., Kuo, L., Masters, P., Vennema, H., & Rottier, P. (1998). Coronavirus Particle Assembly: Primary Structure Requirements of the Membrane Protein. *Journal of Virology, 72*(8), 6838-6850.

[48] Degauque, N., Haziot, A., Brouard, S., & Mooney, N. (2021). Endothelial cell, myeloid, and adaptive immune responses in SARS-CoV-2 infection. *The FASEB Journal*, *35*(5), E21577.

[49] Boumaza, A., Gay, L., Mezouar, S., Bestion, E., Diallo, A., Michel, M., . . . Mege, J. (2021). Monocytes and Macrophages, Targets of Severe Acute Respiratory Syndrome Coronavirus 2: The Clue for Coronavirus Disease 2019 Immunoparalysis. *The Journal of Infectious Diseases*, *224*(3), 395-406.

[50] Descriptive analysis of long COVID sequelae identified in a multidisciplinary clinic serving hospitalised and non-hospitalised patients. (2021). *ERJ Open Research*, *7*(3). https://doi.org/10.1183/23120541.00205-2021

[51] Cascella M, Rajnik M, Aleem A, et al. Features, Evaluation, and Treatment of Coronavirus (COVID-19) [Updated 2022 Feb 5]. In: StatPearls [Internet]. Treasure Island (FL): StatPearls Publishing; 2022 Jan-. https://www.ncbi.nlm.nih.gov/books/NBK554776/

[52] Kang, Dedong, Nakayama, Tomoko, Togashi, Mayuko, Yamamoto, Masuki, Takahashi, Mikiko, Kunugi, Shinobu, Ishizaki, Masamichi, & Fukuda, Yuh. (2009). Two forms of diffuse alveolar damage in the lungs of patients with acute respiratory distress syndrome. *Human Pathology*, *40*(11), 1618–1627. https://doi.org/10.1016/j.humpath.2009.04.019

[53] Bahadur, Kalonia, T., Kamini, K., Gupta, B., Kalhan, S., & Jain, M. (2021). Changes in peripheral blood in SARS CoV-2 patients and its clinico-pathological correlation: A prospective cross-sectional study. *International Journal of Laboratory Hematology*, *43*(6), 1334–1340. https://doi.org/10.1111/ijlh.13720

[54] Lin, Jiang, X., Zhang, Z., Huang, S., Zhang, Z., Fang, Z., Gu, Z., Gao, L., Shi, H., Mai, L., Liu, Y., Lin, X., Lai, R., Yan, Z., Li, X., & Shan, H. (2020). Gastrointestinal symptoms of 95 cases with SARS-CoV-2 infection. *Gut*, *69*(6), 997–1001. https://doi.org/10.1136/gutjnl-2020-321013

[55] Cichoż-Lach, & Michalak, A. (2021). Liver injury in the era of COVID-19. World *Journal of Gastroenterology: WJG, 27*(5), 377–390. https://doi.org/10.3748/wjg.v27.i5.377

[56] Wang, Xiong, H., Chen, H., Li, Q., & Ruan, X. Z. (2021). Renal Injury by SARS-CoV-2 Infection: A Systematic Review. *Kidney Diseases*, *7*(2), 100.

[57] Meinhardt, Radke, J., Dittmayer, C., Franz, J., Thomas, C., Mothes, R., Laue, M., Schneider, J., Brünink, S., Greuel, S., Lehmann, M., Hassan, O., Aschman, T., Schumann, E., Chua, R. L., Conrad, C., Eils, R., Stenzel, W., Windgassen, M., … Heppner, F. L. (2021). Olfactory transmucosal SARS-CoV-2 invasion as a port of central nervous system entry in individuals with COVID-19. *Nature Neuroscience*, *24*(2), 168–175. https://doi.org/10.1038/s41593-020-00758-5

[58] Montgomery, Hong, K., Clarke, K. E. N., Williams, S., Fukunaga, R., Fields, V. L., Park, J., Schieber, L. Z., Kompaniyets, L., Ray, C. M., Lambert, L. A., D'Inverno, A. S., Ray, T. K., Jeffers, A., & Mosites, E. (2022). Hospitalizations for COVID-19 Among US People Experiencing Incarceration or Homelessness. *JAMA Network Open*, *5*(1), e2143407–e2143407. https://doi.org/10.1001/jamanetworkopen.2021.43407

[59] Krammer F (October 2020). SARS-CoV-2 vaccines in development. *Nature*, *586*(7830), 516–527. https://doi.org/10.1038/s41586-020-2798-3

[60] "What are viral vector-based vaccines and how could they be used against COVID-19?". Gavi, the Vaccine Alliance (GAVI). 2020. Retrieved 26 January 2021.

[61] Tregoning, Flight, K. E., Higham, S. L., Wang, Z., & Pierce, B. F. (2021). Progress of the COVID-19 vaccine effort: viruses, vaccines and variants versus efficacy, effectiveness and escape. *Nature Reviews. Immunology*, *21*(10), 626–636. https://doi.org/10.1038/s41577-021-00592-1

[62] Zhou, Xie, Y., Tang, L.-S., Pu, D., Zhu, Y.-J., Liu, J.-Y., & Ma, X.-L. (2021). Therapeutic targets and interventional strategies in COVID-19: mechanisms and clinical studies. *Signal Transduction and Targeted Therapy*, *6*(1), 317–317. https://doi.org/10.1038/s41392-021-00733-x

[63] Spinner, Gottlieb, R. L., Criner, G. J., Arribas López, J. R., Cattelan, A. M., Soriano Viladomiu, A., Ogbuagu, O., Malhotra, P., Mullane, K. M., Castagna, A., Chai, L. Y. A., Roestenberg, M., Tsang, O. T. Y., Bernasconi, E., Le Turnier, P., Chang, S.-C., SenGupta, D., Hyland, R. H., Osinusi, A. O., … Marty, F. M. (2020). Effect of Remdesivir vs Standard Care on Clinical Status at 11 Days in Patients With Moderate COVID-19: A Randomized Clinical Trial. *JAMA: The Journal of the American Medical Association, 324*(11), 1048–1057. https://doi.org/10.1001/jama.2020.16349

[64] Stephens B (18 April 2020). The Story of Remdesivir. *The New York Times*. p. A23. Archived from the original on 22 May 2020. Retrieved 11 May 2020.

[65] HHS Office of the Assistant Secretary for Preparedness and Response (ASPR). (n.d.). *Covid-19 Therapeutics*. COVID-19 Therapeutics | HHS/ASPR. Retrieved

March 1, 2022, from https://aspr.hhs.gov/COVID-
19/Therapeutics/Pages/default.aspx

[66] Administration for Children and Families (ACF). (2022, January 24). *I have covid-
19*. combatCOVID.hhs.gov. https://combatcovid.hhs.gov/possible-treatment-
options-covid-19/i-have-covid-19

[67] Baker, & Dettmer, A. M. (2017). The well-being of laboratory non-human primates.
American Journal of Primatology, *79*(1), e22520.
https://doi.org/10.1002/ajp.22520

[68] Salguero, White, A. D., Slack, G. S., Fotheringham, S. A., Bewley, K. R., Gooch, K.
E., Longet, S., Humphries, H. E., Watson, R. J., Hunter, L., Ryan, K. A., Hall, Y.,
Sibley, L., Sarfas, C., Allen, L., Aram, M., Brunt, E., Brown, P., Buttigieg, K. R.,
… Darby, A. (2021). Comparison of rhesus and cynomolgus macaques as an
infection model for COVID-19. *Nature Communications*, *12*(1), 1260–1260.
https://doi.org/10.1038/s41467-021-21389-9

[69] Chang, M. C., et al. (2021). "Nonhuman primate models for SARS-CoV-2 research:
Consider alternatives to macaques." *Lab Animal 50*(5): 113-114

[70] Callaway. (2020). Dozens to be deliberately infected with coronavirus in UK 'human
challenge' trials. *Nature*, *586*(7831), 651–652. https://doi.org/10.1038/d41586-
020-02821-4

[71] Li, Ye, Z., Zhang, A. J.-X., Chan, J. F.-W., Song, W., Liu, F., Chen, Y., Kwan, M.
Y.-W., Lee, A. C.-Y., Zhao, Y., Wong, B. H.-Y., Yip, C. C.-Y., Cai, J.-P., Lung,
D. C., Sridhar, S., Jin, D., Chu, H., To, K. K.-W., & Yuen, K.-Y. (2022). Severe
acute respiratory syndrome coronavirus 2 (SARS-CoV-2) infections by intranasal
or testicular inoculation induces testicular damage preventable by vaccination in
golden Syrian hamsters. *Clinical Infectious Diseases, 75*(1), e974–e990.
https://doi.org/10.1093/cid/ciac142

72 Gruber, Firsching, T. C., Trimpert, J., & Dietert, K. (2021). Hamster models of
COVID-19 pneumonia reviewed: How human can they be? *Veterinary Pathology*,
30098582110571–3009858211057197.
https://doi.org/10.1177/03009858211057197

[73] Muñoz-Fontela, Dowling, W. E., Funnell, S. G. ., Gsell, P. S., Riveros-Balta, X.,
Albrecht, R. A., Andersen, H., Baric, R. S., Carroll, M. W., Cavaleri, M., Qin, C.,
Crozier, I., Dallmeier, K., Waal, de, Leon, Wit, de, Emmie, Delang, L., Dohm, E.,
Duprex, W. ., Falzarano, D., … Gralinski, L. (2020). Animal models for COVID-
19. *Nature*, *586*(7830), 509–515. https://doi.org/10.1038/s41586-020-2787-6

[74] Rawle, Le, T. T., Dumenil, T., Yan, K., Tang, B., Nguyen, W., Watterson, D., Modhiran, N., Hobson-Peters, J., Bishop, C., & Suhrbier, A. (2021). ACE2-lentiviral transduction enables mouse SARS-CoV-2 infection and mapping of receptor interactions. *PLoS Pathogens*, *17*(7), e1009723. https://doi.org/10.1371/journal.ppat.1009723

[75] Li, Bai, W., & Hashikawa, T. (2020). The neuroinvasive potential of SARS-CoV2 may play a role in the respiratory failure of COVID-19 patients. *Journal of Medical Virology*, *92*(6), 552–555. https://doi.org/10.1002/jmv.25728

[76] Franca, Ugga, L., Guadagno, E., Russo, D., & Del Basso De Caro, M. (2021). Neuroinvasive potential of SARS-CoV2 with neuroradiological and neuropathological findings: is the brain a target or a victim? *APMIS: Acta Pathologica, Microbiologica et Immunologica Scandinavica, 129*(2), 37–54. https://doi.org/10.1111/apm.13092

[77] Speth, Singer-Cornelius, T., Oberle, M., Gengler, I., Brockmeier, S. J., & Sedaghat, A. R. (2020). Mood, Anxiety and Olfactory Dysfunction in COVID-19: Evidence of Central Nervous System Involvement? *The Laryngoscope*, *130*(11), 2520–2525. https://doi.org/10.1002/lary.28964

[78] Pruimboom. (2021). SARS-CoV 2; Possible alternative virus receptors and pathophysiological determinants. *Medical Hypotheses*, *146*, 110368–110368. https://doi.org/10.1016/j.mehy.2020.110368

[79] Mohan, N., Fayyaz, M. A., del Rio, C., Khurana, N. K. R. S., Vaidya, S. S., Salazar, E., Joyce, J., & Ali, A. A. (2021). Neurological manifestations and neuroimaging findings in patients with SARS-CoV2—a systematic review. *The Egyptian Journal of Neurology, Psychiatry and Neurosurgery*, *57*(1), article 68. https://doi.org/10.1186/s41983-021-00322-3

[80] Song, Zhang, C., Israelow, B., Lu-Culligan, A., Prado, A. V., Skriabine, S., Lu, P., Weizman, O.-E., Liu, F., Dai, Y., Szigeti-Buck, K., Yasumoto, Y., Wang, G., Castaldi, C., Heltke, J., Ng, E., Wheeler, J., Alfajaro, M. M., Levavasseur, E., … Iwasaki, A. (2021). Neuroinvasion of SARS-CoV-2 in human and mouse brain. *The Journal of Experimental Medicine*, *218*(3). https://doi.org/10.1084/jem.20202135

[81] Di Liberto, Pantelyushin, S., Kreutzfeldt, M., Page, N., Musardo, S., Coras, R., Steinbach, K., Vincenti, I., Klimek, B., Lingner, T., Salinas, G., Lin-Marq, N., Staszewski, O., Costa Jordão, M. J., Wagner, I., Egervari, K., Mack, M., Bellone, C., Blümcke, I., … Merkler, D. (2018). Neurons under T Cell Attack Coordinate Phagocyte-Mediated Synaptic Stripping. *Cell*, *175*(2), 458–471.e19. https://doi.org/10.1016/j.cell.2018.07.049

[72] Muñoz-Fontela, Dowling, W. E., Funnell, S. G. ., Gsell, P. S., Riveros-Balta, X., Albrecht, R. A., Andersen, H., Baric, R. S., Carroll, M. W., Cavaleri, M., Qin, C., Crozier, I., Dallmeier, K., Waal, de, Leon, Wit, de, Emmie, Delang, L., Dohm, E., Duprex, W. ., Falzarano, D., … Gralinski, L. (2020). Animal models for COVID-19. *Nature*, *586*(7830), 509–515. https://doi.org/10.1038/s41586-020-2787-6

[73] Israelow, Song, E., Mao, T., Lu, P., Meir, A., Liu, F., Alfajaro, M. M., Wei, J., Dong, H., Homer, R. J., Ring, A., Wilen, C. B., & Iwasaki, A. (2020). Mouse model of SARS-CoV-2 reveals inflammatory role of type I interferon signaling. *The Journal of Experimental Medicine*, *217*(12). https://doi.org/10.1084/jem.20201241

CURRICULUM VITAE